AGU PUBLICATIONS

JGR

Journal of Geophysical Research: Solid Earth

RESEARCH ARTICLE
10.1002/2016JB012887

Key Points:
- Various seismic data sets from USArray are collected, processed, and inverted
- A crustal and uppermost mantle model for U.S. is presented
- Systematic and nonsystematic errors in resulting model are investigated

Correspondence to:
W. Shen,
weisen.shen@colorado.edu

Citation:
Shen, W., and M. H. Ritzwoller (2016), Crustal and uppermost mantle structure beneath the United States, *J. Geophys. Res. Solid Earth*, *121*, 4306–4342, doi:10.1002/2016JB012887.

Received 4 FEB 2016
Accepted 2 MAY 2016
Accepted article online 5 MAY 2016
Published online 5 JUN 2016

Crustal and uppermost mantle structure beneath the United States

Weisen Shen[1] and Michael H. Ritzwoller[1]

[1]Department of Physics, University of Colorado at Boulder, Boulder, Colorado, USA

Abstract This paper presents a new model of the shear velocity structure of the crust and uppermost mantle beneath the contiguous U.S. The model is based on more than a decade of USArray Transportable Array (TA) data across the U.S. and derives from a joint Bayesian Monte Carlo inversion of Rayleigh wave group and phase speeds determined from ambient noise and earthquakes, receiver functions, and Rayleigh wave ellipticity (*H/V*) measurements. Within the Bayesian inverse theoretic framework, a prior distribution of models is posited and a posterior distribution is inferred beneath all of the more than 1800 TA stations across the U.S. The resulting mean and standard deviation of the mean of the posterior distribution at each station summarize the inversion results, which are then interpolated onto a regular 0.25°×0.25° grid across the U.S. to define the final 3-D model. We present arguments that show that the standard deviation of the posterior distribution overestimates the effect of nonsystematic errors in the final model by a factor of 4–5 and identify uncertainties in density and mantle *Q* as primary potential sources of remaining systematic error in the final model. The model presents a great many newly resolved structural features across the U.S. that require further analysis and dedicated explication. We highlight here low-velocity anomalies in the upper mantle that underlie the Appalachians with centers of anomalies in northern Georgia, western Virginia, and, most prominently, New England.

1. Introduction

The USArray/Transportable Array (TA), one of the principal components of EarthScope, has been evolving for more than the past 10 years. Since 2004, the TA has repeatedly deployed approximately 400 three-component broadband seismometers at temporary sites with an interstation spacing of about 70 km. The array has crept continuously across the U.S. to occupy sites that have eventually spanned the continent, completing its eastward migration in the fall of 2013. Nearly 2000 independent locations were occupied during the migration of the array. This seismic observatory has stimulated many innovations in seismology designed to improve the understanding of Earth structure and processes beneath the contiguous United States. In particular, crustal imaging at continental scales has been revolutionized in response to the existence of data from this array.

The current paper is based on TA data. Methodologically, this paper is part of a series of research efforts that have attempted to model crustal and uppermost mantle structure beneath the contiguous U.S. using newly developed methods of data analysis, inversion, and inference designed for application to current generation continental array data, of which the TA is a prime example. There have been two principal themes that have guided these efforts: (1) the tracking of uncertainty from measured quantities to resulting 3-D models and (2) assimilating new data types and resources into the inversion as they become available. With the completion of the TA in 2013, models of the crust and uppermost mantle can now be constructed across the entire U.S.

These research efforts have been composed of five principal components on which the current paper builds and of which it is a natural continuation. First, in order to constrain crustal structure, ambient noise surface wave tomography was developed and has been applied to data beginning from the earliest days of operation of the TA [e.g., *Sabra et al.*, 2005; *Shapiro et al.*, 2005; *Bensen et al.*, 2007; *Lin et al.*, 2008]. Ambient noise tomography has become a standard method in crustal imaging and has provided unprecedented information about crustal structure across the U.S. [e.g., *Moschetti et al.*, 2007, 2010a, 2010b; *Yang et al.*, 2008, 2011; *Bensen et al.*, 2009; *Lin et al.*, 2011; *Tian et al.*, 2013; *Xie et al.*, 2015]. The eikonal tomography method was developed to optimize information derived from ambient noise tomography [*Lin et al.*, 2009]. Second, to generate higher-resolution information from surface waves about upper mantle structure, the Helmholtz tomography method was developed for application to data from earthquakes [*Lin and Ritzwoller*, 2011; *Ritzwoller et al.*, 2011; *Mordret et al.*, 2013; *Jin and Gaherty*, 2015] similar to the method of *Pollitz and Snoke* [2010]. Eikonal tomography is a

geometrical ray theoretical method, and Helmholtz tomography is a finite frequency method; finite frequency corrections are needed at the longer periods at which earthquake-generated surface waves are observed. Third, both eikonal and Helmholtz tomography provide information about azimuthal anisotropy and (importantly) local uncertainty estimates of the resulting tomographic maps. Fourth, surface wave data alone typically do not unambiguously constrain vertically discontinuous variations in model variables such as may occur at the base of sedimentary basins or at the Moho. *Lebedev et al.* [2013] present a recent assessment of the problem. It has long been known that the assimilation of other types of data in addition to surface wave dispersion helps to resolve ambiguities that arise in the estimation of crustal and uppermost mantle structure, particularly related to crustal thickness, structure near to the Moho, and near-surface structure [e.g., *Last et al.*, 1997; *Özalaybey et al.*, 1997; *Julia et al.*, 2000]. There are numerous examples of the joint inversion of surface wave data and receiver functions [e.g., *Chang et al.*, 2004; *Lawrence and Wiens*, 2004; *Liu et al.*, 2010; *Tokam et al.*, 2010; *Bodin et al.*, 2012]. We (and others) have developed methods to assimilate other types of data and invert them systematically and jointly along with surface wave dispersion using uncertainty information, including receiver functions [*Shen et al.*, 2013a, 2013b, 2013c], local amplification measurements [*Taylor et al.*, 2009; *Lin et al.*, 2012a; *Eddy and Ekström*, 2014], Rayleigh wave ellipticity (or *H/V*) measurements [*Lin et al.*, 2012b; *Lin and Schmandt*, 2014; *Lin et al.*, 2014], and body waves [*Obrebski et al.*, 2011; *Porritt et al.*, 2014]. Fifth, Bayesian Monte Carlo inversion methods have been developed [e.g., *Shen et al.*, 2013a, 2013b, 2013c] to invert jointly new high-resolution surface wave dispersion information together with other data types in order to produce distributions of models that fit all data acceptably. The resulting posterior distributions of models are then summarized to produce the 3-D model together with uncertainties.

The TA has stimulated a variety of approaches to inferring information about crustal and mantle structure beneath the U.S. For example, the current paper is one of many based at least in part on ambient noise observations across the U.S., e.g., *Liang and Langston* [2008, 2009], *Prieto and Beroza* [2008], *Ma et al.* [2008], *Gao et al.* [2011], *Calkins et al.* [2011], *Porritt et al.* [2011], *Delorey and Vidale* [2011], *Gaite et al.* [2012], *Liu et al.* [2012], *Tibuleac and von Seggern* [2012], *Gao and Shen* [2012], *Hansen et al.* [2013], *Allison et al.* [2013], *Kao et al.* [2013], *Boué et al.* [2014], *Li and Lin* [2014], *Porter et al.* [2014, 2015], *Yang* [2014], *Ekström* [2014], *Schmandt and Lin* [2014], *Fu and Li* [2015], *Zigone et al.* [2015], *Agrawal et al.* [2015], and others. The measurement of Rayleigh wave ellipticity (or *H/V* measurements) using earthquake data goes back to *Boore and Toksoz* [1969] and has been recently rejuvenated by *Tanimoto and Rivera* [2008] and *Lin et al.* [2012b]. *Lin et al.* [2014] extended the *H/V* measurements to ambient noise, and *Lin and Schmandt* [2014] also extended them to azimuthal anisotropy. *Lin et al.* [2012b] performed a joint inversion of *H/V* measurements along with surface wave dispersion for crustal and uppermost mantle structure. In addition, there have been many studies of both *P*-to-*S* and *S*-to-*P* receiver functions across the U.S. based at least in part on USArray data [e.g., *Agrawal et al.*, 2015; *Benoit et al.*, 2014; *Calkins et al.*, 2010; *Eagar et al.*, 2011; *Frassetto et al.*, 2011; *Gao*, 2015; *Gashawbeza et al.*, 2008; *Gilbert*, 2012; *Hansen and Dueker*, 2009; *Hansen et al.*, 2013; *Hopper et al.*, 2014; *Levander and Miller*, 2012; *Levander et al.*, 2011; *Parker et al.*, 2013; *Porter et al.*, 2014; *Stachnik et al.*, 2008; *Thurner et al.*, 2015; *Wagner et al.*, 2012; *Wilson et al.*, 2010; *Yeck et al.*, 2014].

The joint inversion of surface wave dispersion, receiver functions, and Rayleigh wave *H/V* measurements remains rare. To the best of our knowledge using USArray data the joint inversion of surface wave dispersion together with receiver functions in the U.S. has been carried out regionally only by *Bailey et al.* [2012] and *Shen et al.* [2013a, 2013b, 2013c] and the joint inversion of surface wave dispersion together with *H/V* measurements by *Lin et al.* [2012b]. The joint inversion of all three data sets has not been performed before in the U.S. but has been accomplished in a regional study in China [*Kang et al.*, 2016]. The current paper is a natural continuation of the studies of *Shen et al.* [2013a, 2013b, 2013c], which developed and applied Bayesian Monte Carlo inversion methods to the joint inversion of Rayleigh wave dispersion from ambient noise and earthquake data and receiver function data across the western half of the U.S. The current paper modifies and extends this earlier work by introducing a new data set of Rayleigh wave *H/V* measurements across the entire U.S. and inverting all data simultaneously (Rayleigh wave dispersion from 8 to 90 s period, receiver functions, and Rayleigh wave *H/V* measurements from 18 to 80 s period) to estimate a unified crustal and uppermost mantle model across the entire contiguous U.S. with attendant uncertainties. More than 5 years of TA data are added, and the region of study extends about 3000 km farther east compared to the earlier studies of *Shen et al.* [2013b]. In total, we obtain observations using ~1800 TA stations deployed before June 2015 that spans a variety of tectonic features of the contiguous US (Figure 1 and Table 1) and invert all data within a Bayesian Monte Carlo framework.

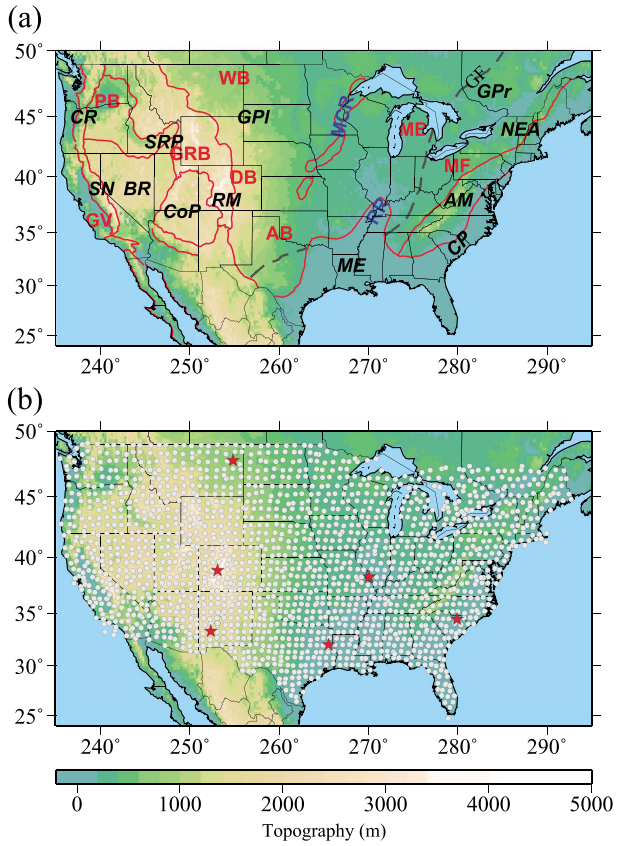

Figure 1. Area of study, geographic and tectonic features, and station coverage. (a) Map of the contiguous U.S. with major physiographic boundaries [*Fenneman and Johnson*, 1946] shown with red lines. Black abbreviations note the names of tectonic regions; blue abbreviations identify the two rifts; red symbols denote the sedimentary basins; and the black dashed line, divided by the Mississippi Embayment, marks the location of the Grenville Front (GF). Location names are identified in Table 1. (b) Stations used in this study are shown as gray circles. Red stars mark the locations of the six example stations whose data and inversion results are shown later in the paper: Z21A near Winston, NM; Q22A near Crested Butte, CO; C23A near Lambert, MT; 239A near Gary, TX; R43A near Red Bud, IL; and X57A near Hartsville, SC.

Significantly, consistent with the findings of *Shen et al.* [2013a, 2013b], the introduction of receiver functions into the inversion significantly improves determination of Moho depth and structures near the crust-mantle transition, and consistent with the findings of *Lin et al.* [2012b], the introduction of the *H/V* measurements significantly improves estimates of structures in the top few kilometers of the crust. Overall, combining all three data sets improves the vertical resolution of the crust and uppermost mantle, and the resulting 3-D V_s model reveals high-fidelity features of the crust and uppermost mantle across the entire U.S.

The discussion below begins with a description of the data set of Rayleigh wave dispersion measurements, receiver functions, and Rayleigh wave *H/V* measurements in section 2. Although the full data set is new, the methods of measurement have been described elsewhere, and here we only summarize the methods used to estimate the principal quantities and errors in them. The joint Bayesian Monte Carlo inversion method also has been described elsewhere. Only salient aspects of the method are summarized in section 3, where we focus attention on the description of the assumptions and constraints that result in the prior distribution of models at each location. The Bayesian Monte Carlo method jointly inverts all data, producing a posterior distribution of models at each of more than 1750 stations across the U.S. In section 4, we discuss how we summarize these distributions in terms of a mean and standard deviation at each depth in the crust and uppermost mantle and location across the U.S. and how the mean varies regionally and within regions across the U.S. We discuss how the posterior distribution can be used to quantify the effects of random errors in the model. In section 5, we present vertical transects of the model and discuss systematic errors that may arise due to constraints and assumptions applied in the inversion.

2. Data: Measurement, Processing, and Uncertainty

This study is based on data from the 1822 (virtual) USArray Transportable Array seismic stations that are shown in Figure 1b. These stations are fairly homogeneously distributed across the U.S., being spaced on average about every 70 km. Based on data from these stations, we produce (1) Rayleigh wave dispersion maps and local dispersion curves from ambient noise and earthquake data, (2) azimuthally independent receiver functions, and (3) Rayleigh wave ellipticity measurements, also referred to as *H/V* measurements [e.g., *Lin et al.*, 2012b]. We construct Rayleigh wave phase speed curves from 8 to 90 s period beneath each station from dispersion maps produced by eikonal tomography [*Lin et al.*, 2009] for ambient noise data and Helmholtz tomography [*Lin and Ritzwoller*, 2011] for teleseismic earthquake data. We generate Rayleigh wave group velocity curves by traditional ray theoretic tomography [*Barmin et al.*, 2001; *Moschetti et al.*, 2010a] between periods of 8 s and 40 s. In addition, we construct a back azimuth-independent receiver function using

Table 1. Abbreviations of Tectonic Features and Geographic Names Marked in Figures 1, 21, and 22

Sedimentary basins	AB	Anadarko Basin
	DB	Denver Basin
	GRB	Green River Basin
	GV	Great Valley
	MB	Michigan Basin
	MF	Marcellus Formation
	PB	Pasco Basin
	WB	Williston Basin
Tectonic features	AB	Anadarko Basin
	AM	Appalachian Mountains
	BR	Basin and Range
	CoP	Colorado Plateau
	CP	Coastal Plains
	CR	Cascade Range
	GPl	Great Plains
	GPr	Grenville Province
	MCR	Mid-Continent Rift
	ME	Mississippi Embayment
	NEA	Northeastern Appalachians
	RGR	Rio Grande Rift
	RM	Rocky Mountains
	RR	Reelfoot Rift
	SN	Sierra Nevada
	SRP	Snake River Plain
	WC	Wyoming Craton
	YS	Yellowstone
Geographic names	GA	Georgia
	IL	Illinois
	NE	New England
	OH	Oklahoma
	PA	Pennsylvania
	VA	Virginia

the harmonic stripping technique [*Shen et al.*, 2013a] at each station. The details of the data processing and subsequent data quality control and refinement have been documented in a number of previous papers, and we only briefly summarize the data processing here.

2.1. Rayleigh Wave Phase Velocities

We obtained Rayleigh wave phase time (or speed) measurements between periods of 8 and 40 s using ambient noise cross correlations between data from USArray TA stations available from January 2005 to the end of June 2015 using automated frequency-time analysis (AFTAN) [e.g., *Levshin and Ritzwoller*, 2001; *Bensen et al.*, 2007]. The ambient noise data processing follows the procedure described by *Bensen et al.* [2007] and *Lin et al.* [2008]. More than 650,000 cross correlations across the study region are produced. At short periods (8 to 40 s), we apply eikonal tomography [*Lin et al.*, 2009] to the ambient noise phase travel time measurements to generate Rayleigh wave phase velocity maps with uncertainty estimates (e.g., Figures 2c and 2d). At longer periods (28 to 80 s), we apply the Helmholtz tomography method [*Lin and Ritzwoller*, 2011] to the earthquake-derived phase travel time measurements from AFTAN to obtain Rayleigh wave phase velocity measurements with uncertainties. Both eikonal and Helmholtz tomography estimate local uncertainties in phase speed from the scatter in the local azimuthally dependent phase times (and thus speeds) after smooth variations with azimuth are removed. The standard deviation of the mean of the observed scatter is then identified with the error in the local period-dependent phase speed. Rayleigh wave phase travel times are measured using waveform data following 5898 earthquakes recorded between 2005 and 2015 with $M_s > 5.5$, and Helmholtz tomography is applied to produce the phase velocity maps. The Helmholtz tomography method provides a finite frequency correction, which is needed at long periods, but the eikonal tomography method (applied at shorter periods) does not. Sample maps are presented in Figures 2e and 2f. In the period band in which ambient noise and earthquake measurements overlap (28 to 40 s), there is significant agreement between the maps. Several earlier studies found that phase speed measurements inferred from earthquakes were somewhat faster than those from ambient noise measurements [*Yao et al.*, 2006; *Yang et al.*, 2008]. As we have added increasing numbers of earthquake measurements, however, measurements from earthquakes have converged to those from ambient noise [*Lin and Ritzwoller*, 2011; *Ritzwoller et al.*, 2011], such that, now at 28 s period, for example, the average difference across the U.S. is about 1 m/s. The standard deviation of the difference is about 12 m/s, which is within the estimated average uncertainty (~15 m/s). *Ritzwoller et al.* [2011] presents a map demonstrating the high quality of agreement between the 30 s Rayleigh wave phase speed maps derived from ambient noise and earthquakes using eikonal tomography. In both eikonal tomography applied to ambient noise data and Helmholtz tomography applied to earthquake data, azimuthal anisotropy with 180° symmetry is estimated simultaneously with azimuthally independent phase speeds. Thus, the effect of azimuthal anisotropy has been removed from the isotropic phase speed measurements presented here.

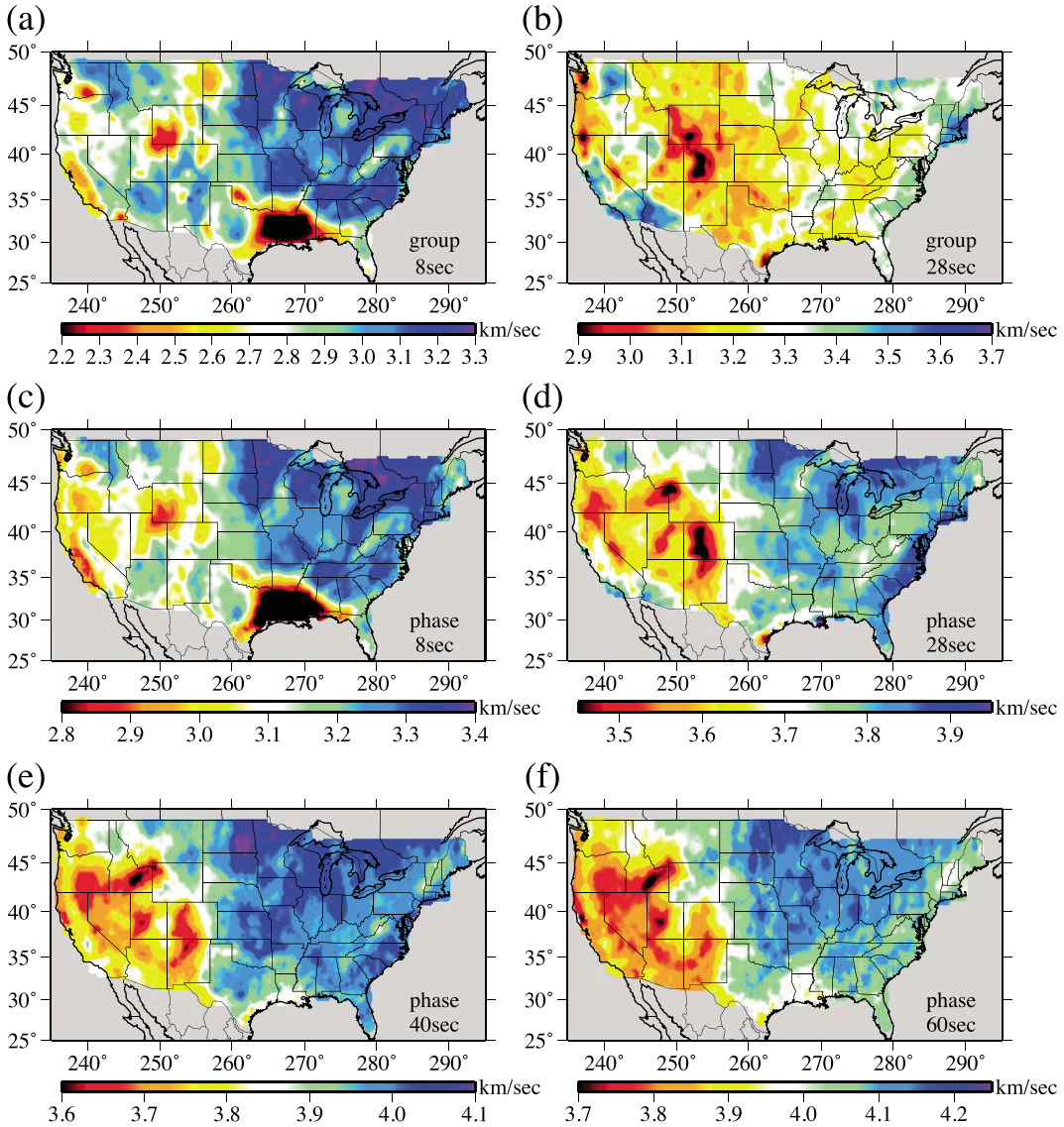

Figure 2. Rayleigh wave group and phase speed maps. (a and b) Group velocity maps at 8 and 28 s produced from ambient noise straight-ray tomography, respectively. (c and d) Phase velocity maps at 8 and 28 s produced from ambient noise eikonal tomography, respectively. (e and f) Phase velocity maps at 40 and 60 s produced from earthquake Helmholtz tomography, respectively.

2.2. Rayleigh Wave Group Velocities

Both phase and group velocity dispersion curves are measured when automated frequency-time analysis (AFTAN) is applied to ambient noise cross correlations. Although eikonal tomography is performed on the phase time measurements from ambient noise, the eikonal equation governs the propagation of phase but not group times. Thus, we use the traditional damped least squares tomographic method of *Barmin et al.* [2001] for group velocities. The traditional tomographic method and eikonal tomography provide similar results for phase speeds, as shown by *Lin et al.* [2009] and *Zhou et al.* [2012], which gives us confidence in the use of the traditional method for group speeds. We ignore finite frequency effects on group speeds here, because they are weak in the period band in which ambient noise is considered (8–40 s [e.g., *Lin and Ritzwoller*, 2011; *Ritzwoller et al.*, 2011]). Azimuthal anisotropy with 180° symmetry is estimated simultaneously with azimuthally independent group speeds. Thus, as with phase speeds, the effect of azimuthal anisotropy has been removed from the isotropic group speeds presented here.

The 8 and 28 s period group velocity maps are presented in Figures 2a and 2b. At 8 s period, group velocity is most sensitive to shear wave speed in the top 10 km of the crust. Similar to the 8 s phase velocity map, major basins exhibit slow group velocities (<2.4 km/s). At 28 s period, the group velocity map presents a slightly different pattern than the phase velocity map because of the relatively shallower sensitivity of group velocities. Because a damped least squares inversion is used to generate the group velocity maps, meaningful uncertainties are not obtained in the inversion, although resolution is estimated. The uncertainty of group velocity is scaled from the uncertainty of phase velocity using the relationship described by *Moschetti et al.* [2010b]. On average, group velocity uncertainty is magnified by a factor of about 3 compared with phase velocity uncertainty. In this study, we use group velocity measurements only when the horizontal resolution is better than 100 km; thus, group velocity measurements at some periods are discarded near the edges of the study region. Finally, we obtain local dispersion curves for 1816 out of 1822 USArray/TA stations, and examples of local Rayleigh wave group and phase velocity curves are presented in Figure 3.

2.3. Receiver Functions

Shen et al. [2013b] describe the method that we apply to process receiver functions for each station. For each station, we select earthquakes from January 2005 to June 2015 with epicentral distances ranging between 30° and 90° and with magnitudes $m_b > 5.5$. We apply a time domain deconvolution method [*Ligorria and Ammon*, 1999] to each seismogram windowed between 20 s before and 30 s after the direct *P* wave arrival to compute the radial component receiver function using a low-pass Gaussian filter with a width of 2.5 s (pulse width~1 s). High-quality receiver functions are selected with an automated procedure. Corrections are made both to the time and amplitude of each receiver function, normalizing to a reference slowness of 0.06 s/km [*Jones and Phinney*, 1998]. Finally, we retain only the first 10 s after the direct *P* arrival. We compute the azimuthally independent receiver function, $R_0(t)$, at each station by fitting a truncated Fourier series at each time over azimuth and then stripping the azimuthally variable terms using a method referred to as "harmonic stripping" by *Shen et al.* [2013b]. After removing the azimuthally variable terms at each time, the RMS residual over azimuth is interpreted as the 1σ uncertainty in $R_0(t)$ at that time. On average, 84 individual receiver functions from different earthquakes are accumulated for each station. If fewer than 10 receiver functions pass quality control at a particular station, we do not use the receiver function in the joint inversion. In total, we obtain azimuthally independent receiver functions for 1805 of the 1822 USArray/TA stations. Example receiver functions are presented in Figure 3.

2.4. Rayleigh Wave Ellipticity (*H*/*V*)

As discussed in section 2.1, the data following more than 5800 teleseismic earthquakes are collected to perform teleseismic Helmholtz tomography across the contiguous U.S. This data set is also used to measure the Rayleigh wave *H*/*V* ratio following the processing procedure presented by *Lin et al.* [2012a], which we summarize briefly here.

For each earthquake recorded at each available station, three-component seismograms are cut according to the Rayleigh wave group travel time predicted by a global model [*Shapiro and Ritzwoller*, 2002], and the mean, linear trend, and the station response are removed. The horizontal components (*E* and *N*) are then rotated into the radial (*R*) and transverse (*T*) directions defined by the great circle path between the earthquake and the station. Automated frequency-time analysis, AFTAN [*Bensen et al.*, 2007], is applied to determine the Rayleigh wave phase and group travel times, and the amplitudes of both the vertical (*V*) and radial components are measured between 18 and 80 s period. In essence, a group velocity filter is applied to extract the Rayleigh wave on both the vertical and radial components. A series of narrowband Gaussian filters is applied to each component in the frequency domain, the result is back transformed to the time domain, and the amplitude as a function of the central period of the Gaussian filter is measured in the time domain for both components. The amplitude ratio between the two components (*R*/*V*) is used to evaluate the *H*/*V* ratio as a function of period at the station location.

To insure the quality of the *H*/*V* measurements, we impose the following five control criteria. First, the signal-to-noise ratio must be greater than 15 for Rayleigh waves on both the radial and vertical components. Second, Rayleigh waves on the radial and vertical components are expected to be phase shifted by 90°. Thus, we apply a phase difference criterion: measurements with $|\varphi_R(T) - \varphi_V(T) - \pi/2|(T/2\pi) > 2$ s are removed, where φ_R and φ_V are the observed phase of the radial (*R*) and vertical (*V*) components, respectively, and *T* is

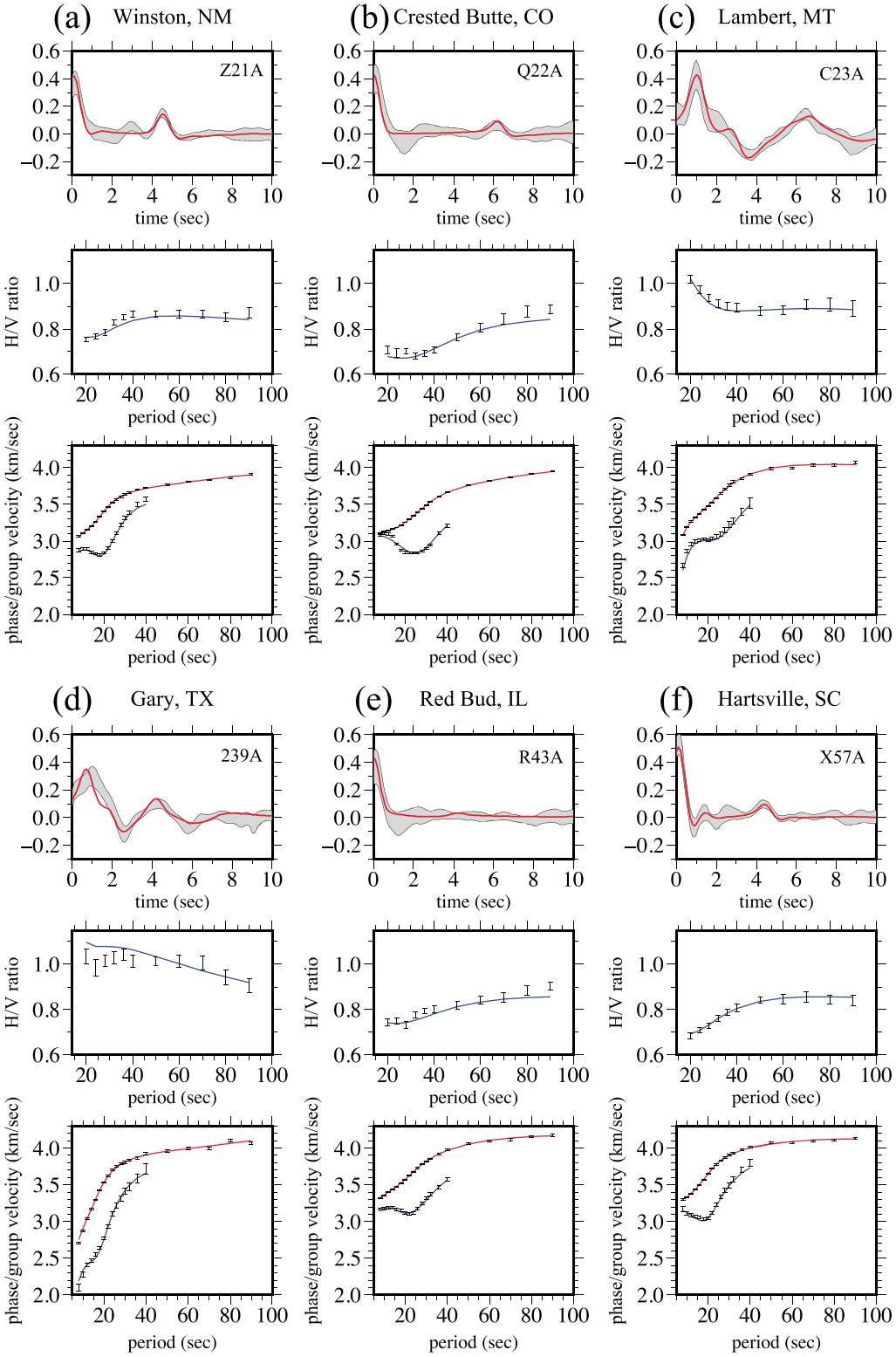

Figure 3. Example data from the (a–f) six locations identified with red stars in Figure 1. For each location three vertically arrayed panels show the three data types: (top) the receiver function is shown with a gray corridor (1 standard deviation error around the mean at each time), (middle) Rayleigh wave *H/V* measurements are shown with 1 standard deviation error bars, and (bottom) Rayleigh wave phase and group velocities (phase speeds are faster than group speeds at each period here) are presented with 1 standard deviation error bars. Solid lines in each panel are the local predictions from the best fitting model in the posterior distribution derived from the joint inversion of all three data sets.

Table 2. Stations With Amplitude Errors

Type of Amplitude Errors	Stations
Half-amplitude error (differential output)	MSO, J17A, N02C, S43A, T41A, 634A, I50A
Other amplitude errors	VES, VMZ, SCZ2

the period of the measurement. Third, group travel times measured on the vertical and radial components must be within $T/2$ s. Fourth, large H/V measurements (>10) are removed. These criteria are applied independently to each station at each period. A final, fifth criterion is invoked in which we estimate the standard deviation, σ, of the measurements at each station and at each period that satisfy the first three selection criteria. To stabilize the measurements, we discard measurements outside the 2σ corridor of measurements.

After these quality control steps, a set of H/V ratio measurements is obtained for each period at each station. For sets with $\geq$20 measurements, the mean and standard deviation of the mean are computed to represent the H/V ratio measurement and its uncertainty at this period and station. We discard measurements at a station if the number of measurements is less than 20 in order to enhance the reliability of the data set. At each station, the H/V measurements estimated from different events are similar, although small variations ($<$2%) dependent on back azimuth are observed. However, for about 15 stations the H/V ratio measurements possess large variations ($>$20%) over time. Conversations with Incorporated Research Institutions for Seismology (IRIS) Data Management Center staff members (personal communication with Robert Busby, IRIS) suggest that these variations are probably due to a differential signal output error of the seismometer sensors. Table 2 lists these 11 stations with the time periods of malfunction. Some of the H/V ratio measurements obtained during the malfunction periods can be corrected, whereas others must be discarded.

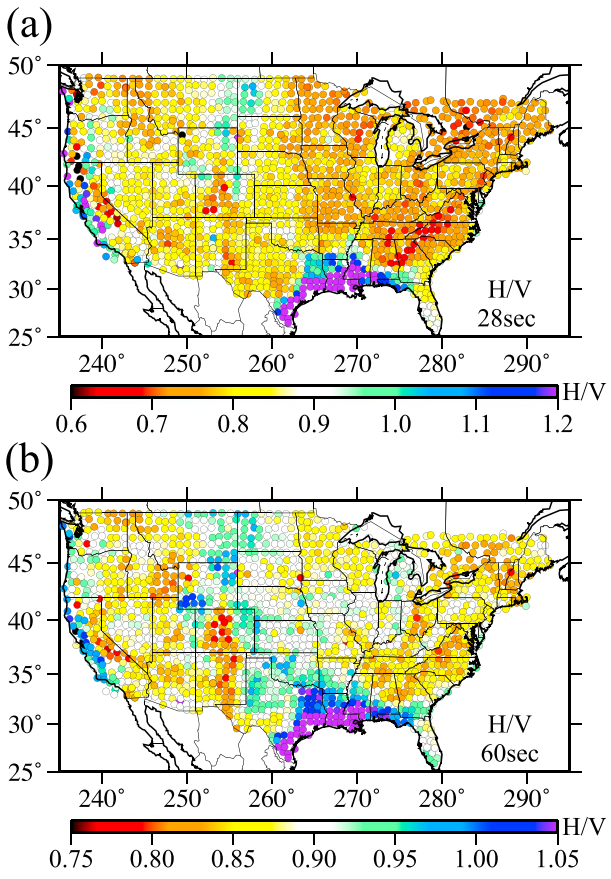

Figure 4. Rayleigh wave H/V ratio measurements at 28 and 60 s, respectively, presented at the stations where they are observed.

Example H/V maps at periods of 28 and 60 s are presented in Figure 4. They are similar to the maps shown by *Lin et al.* [2012a], but the H/V ratios presented here are smaller on average and extend over a larger area. At 28 s period, high H/V ratio is correlated with the sedimentary basin distribution across the continental U.S. (e.g., the Central Valley in California, the Williston Basin near eastern Montana and western North Dakota, and the coastal basins near the Mississippi Embayment). Low H/V ratio is observed in major mountain ranges (e.g., the Sierra Nevada and Rocky Mountains) in the western U.S., in the Superior Upland Province, and the Appalachian Highlands in the eastern U.S., all regions devoid of thick unconsolidated sediments. Beneath the Yellowstone hot spot and southern Sierra Nevada, the lowest H/V measurements across the continent ($<$0.65) are observed. At longer periods, the H/V ratio is still largely sensitive to shallow V_s structure. Figure 24 later in the paper presents sensitivity kernels that demonstrate this. Thus, the effect from major basins is still observed at long periods: the Green River Basin in southwestern Wyoming and the Mississippi Embayment areas possess the highest H/V measurements at this period. The sensitivity kernel of the H/V measurement penetrates into the mantle at long

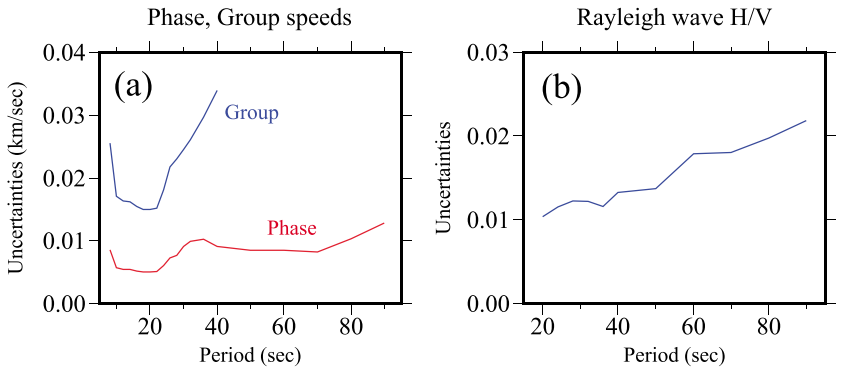

Figure 5. Estimated measurement uncertainties (1σ) as a function of period averaged across the U.S. (a) Raleigh wave group and phase speed uncertainties are presented as a function of period. Group speed uncertainties are derived from ambient noise tomography between 8 and 40 s period, and phase speed uncertainties are from ambient noise at periods from 8 and 26 s, a combination of ambient noise and earthquake tomography from 28 to 36 s period, and earthquake tomography from 40 to 90 s period. (b) Uncertainty in Rayleigh wave *H/V* measurements presented as a function of period from 20 to 90 s. Dispersion uncertainties minimize around 20 s period and grow toward shorter and longer periods. Uncertainties in *H/V* measurements grow approximately linearly with period.

periods and is positively correlated with V_{sv}, so low *H/V* ratio is also observed beneath the Rocky Mountains and the Snake River Plain where the mantle V_{sv} is low (Figure 2f).

Although our quality control procedure has been designed to produce high-quality *H/V* measurements, *H/V* measurements may still be biased due to at least two factors. First, noise tends to be higher on the horizontal than vertical components, which tends to bias *H/V* high. We attempt to use only high SNR measurements on both the vertical and radial components to mitigate this effect. However, further efforts to measure noise levels and correct the resulting *H/V* measurements for the effects of noise may be worthwhile. Second, off-great circle propagation tends to bias the horizontal amplitude and hence *H/V* low. *Pedersen et al.* [2015] presents evidence that period-dependent average absolute deviations from 3° to 9° are probably common, with larger deviations at shorter periods and considerably larger deviations possible. In eikonal and Helmholtz tomography we also measure the angle of approach. Consistent with *Pedersen et al.* [2015] we find that at the six stations presented in Figure 3, the average absolute deviation from the great circle azimuth is about 6° at 30 s period. Variations in the deviation of great circle paths will scatter the *H/V* measurements, but a 6° average deviation at a station would produce *H/V* biased low by about 0.5%. Thus, irrespective of the quality control procedures, our *H/V* measurements may be biased low by more than 0.5%, although a bias at this level does lie within our uncertainty estimates (which average from 1% to 3%; as discussed in section 2.5). In the future it would be advisable to consider correcting the amplitude of the horizontal component for apparent angle of approach. These two effects, higher noise on the horizontal than vertical component and off-great circle propagation, will tend to offset one another, but even greater attention to reducing potential bias in the future is advisable. We construct *H/V* ratio curves for 1779 stations between periods of 20 and 90 s. Several typical *H/V* ratio curves with uncertainties are presented in Figure 3.

2.5. Measurement Uncertainties

We obtain estimates of uncertainties (or errors) for all types of measurements employed here: Rayleigh wave group and phase velocity maps, receiver functions, and local Rayleigh wave *H/V* ratios. Measurement errors averaged spatially across the U.S. are shown in Figure 5 for Rayleigh wave dispersion and *H/V* measurements. Rayleigh wave phase speed measurement errors for both ambient noise and earthquake data are typically less than about 10 m/s (Figure 5a), which is about 0.25% of the phase speed. For an interstation path of 1000 km and a travel time of about 250 s, this is about a half-second measurement error, which is largely independent of period. Further improvements in surface wave tomography designed to beat down this error are needed and would be particularly useful to improve estimates of azimuthal anisotropy. For ambient noise, errors in group velocity maps are scaled from phase velocity errors as discussed in section 2.2. Group speed errors average about 3 times phase speed errors [*Moschetti et al.*, 2010b], but, as Figure 5a shows, above 25 s period phase speed errors remain low even as group speed errors grow rapidly. This is because we

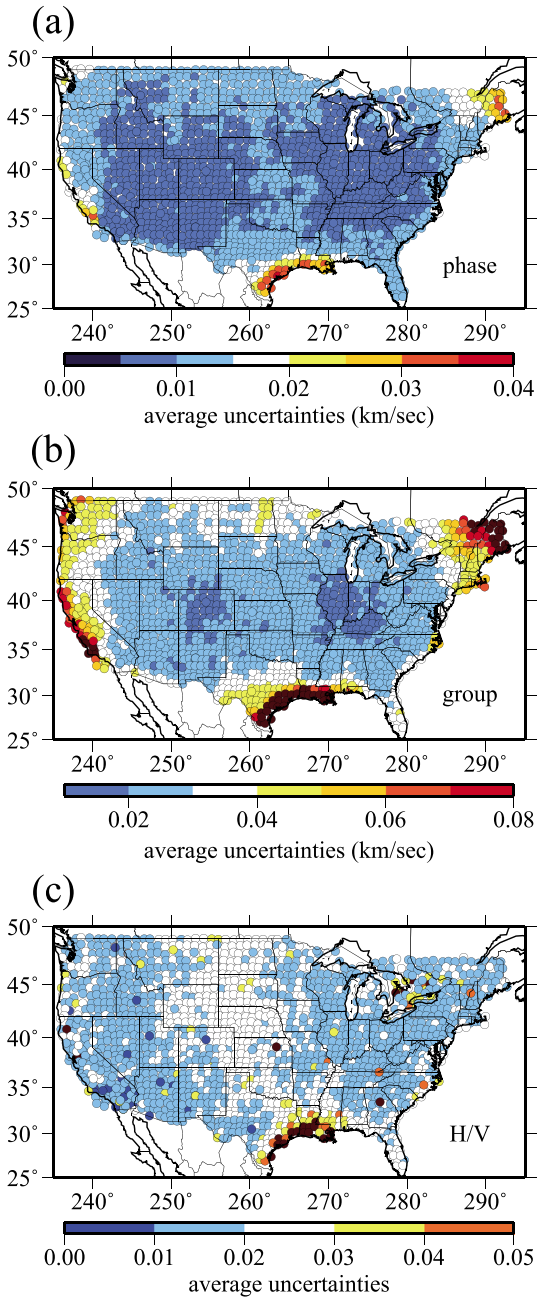

Figure 6. Period averaged measurement uncertainty (1σ) as a function of spatial location. (a) Phase speed uncertainties averaged from 8 to 90 s period. (b) Group speed uncertainty averaged from 8 to 40 s period. (c) Raleigh wave *H/V* measurement uncertainty averaged from 20 to 90 s period. Uncertainties in all observables are fairly homogeneous spatially but grow near the periphery of the array.

introduced earthquake-derived measurements of phase speed at longer periods. Spatially averaged estimates of Rayleigh wave *H/V* errors are presented in Figure 5b. Because *H/V* measurements typically lie between 0.6 and 1.2 (Figure 4), uncertainties in *H/V* measurements typically range from about 1% to 3% of the *H/V* value. We do not present a plot of the average error in receiver functions, but several typical receiver functions with uncertainties are shown in Figure 3. Our receiver function error estimates are conservative, and therefore, we do not attempt to fit small wiggles in the receiver functions.

The spatial variability of period-averaged measurement uncertainties is presented in Figure 6 for Rayleigh phase speed, group speed, and *H/V* ratio. Phase and group speed uncertainties are fairly homogeneous spatially but degrade near the periphery of the study region where azimuthal coverage is suboptimal. For *H/V* measurements, uncertainties are also spatially quite homogeneous but are slightly higher in the Central U.S. than in the western or eastern U.S. because fewer earthquakes are observed there.

2.6. Example Data

As discussed in section 3, we invert data at each station individually. Receiver functions and Rayleigh wave *H/V* measurements are obtained independently at each station. However, dispersion maps are produced on a spatial grid that extends between stations, but we interpolate them to station locations so as to produce station-specific dispersion curves. Thus, at the vast majority of stations across the U.S., we have Rayleigh wave group and phase speed curves as well as a Rayleigh wave *H/V* curve and a receiver function, together with uncertainty estimates of all quantities. Examples of such station-specific data are presented in Figure 3 for the six stations identified in Figure 1b with red stars. Rayleigh wave data are presented on a discrete grid of periods with 1σ error bars. Receiver functions are presented in terms of a gray corridor, which also represents the 1σ uncertainty at each time.

Much information about local structure can be seen directly in the data in Figure 3. For example, the reverberations in the receiver function, high *H/V* values at short periods, and slow short-period group velocities reveal that the stations at Lambert, MT, and Gary, TX, lie in sedimentary basins. The strong Moho *P*-to-*S* phase conversion near 4.5 s on the receiver function at Winston, NM, indicates that there is a sharp Moho there. A later *P*-to-*S* conversion at Crested Butte, CO, indicates a deeper Moho than at Winston, NM. The location of the Airy phase on the group velocity curve at longer periods than at Winston, NM, similarly is consistent with a deeper crust. The relatively flat receiver function at Red Bud, IL, indicates a gradient or

Table 3. Range of Perturbations to Model Variables

Model Variable	Range of Perturbation
Thickness, sedimentary layer	±100%
Thickness, crystalline crust	±20%
V_{sv}, top of sedimentary layer	±1 km/s
V_{sv}, bottom of sedimentary layer	±1 km/s
B-spline coefficients, crust	±20%
B-spline coefficients, mantle	±20%

perhaps complicated Moho structure, which is consistent with a relatively shallow (nearly horizontal) Airy phase on the group velocity curve.

3. Joint Bayesian Monte Carlo Inversion

We describe here the joint Bayesian Monte Carlo inversion. The inversion procedure is very similar to that applied by *Shen et al.* [2013a, 2013b, 2013c] to Rayleigh wave dispersion and receiver functions, except here the joint inversion is extended to incorporate measurements of Rayleigh wave *H/V* ratios in three steps. In the first step, we perform an initial Monte Carlo inversion without the involvement of receiver functions and the *H/V* ratio measurements. Such an inversion produces a model of the crust and uppermost mantle V_{sv} for the contiguous U.S. based on surface wave dispersion alone. We refer to this as the surface wave (SW) inversion. In the second step, we introduce receiver function data and *H/V* measurements. Figure 3 presents example fits to the data for six stations and demonstrates the compatibility of the three data sets that are inverted under the Bayesian Monte Carlo framework. The solid lines in each plot of Figure 3 show predicted data from the best fitting model of the posterior distribution of models that results from the joint inversion. In this step the 3-D model is constrained by all three types of data ("All Data"). The model is determined from the posterior distribution of accepted models beneath each station, and model uncertainties are related to the spread of the posterior distribution. We only perform the inversion at 1750 stations (out of 1822) where we have surface wave dispersion, Rayleigh wave H/V measurements, and receiver functions. In the third and final step, the model produced in the second step is interpolated onto a 0.25° × 0.25° grid by simple kriging.

3.1. Model Specification

At present, the only surface wave data we use are Rayleigh waves (and not Love waves), which are primarily sensitive to V_{sv}. Thus, although we assume the model to be isotropic, $V_{sv} = V_{sh} = V_s$, and we refer to the model as a V_s model, it is actually a V_{sv} model. The V_s model beneath each station is stratified into three principal layers in which V_s changes smoothly vertically. The top layer is the sedimentary layer defined by three unknowns: layer thickness and V_s at the top and bottom of the layer with V_s increasing linearly with depth. The second layer is the crystalline crust, parameterized with five unknowns: four cubic B-splines and crustal thickness. Finally, there is the uppermost mantle layer with five cubic B-splines, yielding a total of 13 free parameters at each location. We have chosen the number of B-splines subjectively to insure that V_s changes smoothly with depth in the crust and mantle but not so smoothly that the data cannot be fit. In addition, as discussed in the next paragraph, V_s will be constrained to increase monotonically with depth in the crust. We set the thickness of the uppermost mantle layer so that the total thickness of all three layers is 200 km. For the initial surface wave (SW) inversion, the model space is based on perturbations to a reference model consisting of the 3-D model of *Shapiro and Ritzwoller* [2002] for crustal V_s, crustal thickness, and mantle V_s. The initial sedimentary model is from *Mooney and Kaban* [2010]. Table 3 presents a summary of the range of perturbations to model variables allowed in the inversion.

In addition, the following three prior constraints are imposed during the Monte Carlo sampling of model space: (1) V_s increases with depth across the two model discontinuities at the base of the sediments and Moho; (2) V_s increases monotonically with depth in the crystalline crust; and (3) at all depths, $V_s < 4.9$ km/s. These constraints are viewed as hypotheses to be tested. In the sedimentary layer, we scale V_p and density from V_s according to *Brocher* [2005]:

$$V_p = 0.941 + 2.095V_s - 0.821{V_s}^2 + 0.268{V_s}^3 - 0.0251{V_s}^4, \quad (1)$$

$$\rho = 1.227 + 1.53V_s - 0.837{V_s}^2 + 0.207{V_s}^3 - 0.0166{V_s}^4, \quad (2)$$

where we have rounded here to three significant figures. This scaling relationship makes the V_p/V_s ratio greater than 2 in the sedimentary layer where $V_s < 3$ km/s. In the crystalline crust and uppermost mantle, the V_p/V_s ratio is fixed to be 1.75. Equation (2) is also used for density in the crystalline crust. In the mantle, density is scaled from V_s perturbations relative to 4.5 km/s with 10 kg/m^3 per 1% velocity change [*Hacker and Abers*, 2004]. The *Q* model from the Preliminary Reference Earth Model (PREM) [*Dziewonski and Anderson*, 1981] is used in

the sedimentary layer and crystalline crust to apply the physical dispersion correction [*Kanamori and Anderson*, 1977], and each resulting model is reduced to 1 s period. Shear Q in the mantle is set to be 150 across the entire study region and with depth. A single value of Q is chosen for simplicity, so that the effect of the choice of Q on the model can be determined easily (cf. section 5.3). The value of 150 is chosen to be intermediate between the lower values expected across much of the western U.S. and the higher values expected across the eastern U.S.

These choices reduce the volume of model space searched, but if they are inaccurate (as they will be at some locations), they will impose a systematic error on the resulting models. Systematic errors are discussed in section 5.3 and compared with random error, which we discuss in section 4.2.

3.2. Prior and Posterior Distributions

Shen et al. [2013b] describe the Bayesian Monte Carlo joint inversion method in detail. The method is influenced strongly by *Mosegaard and Tarantola* [1995]. We only provide a cursory summary here and concentrate on the presentation of the results. The joint inversion method constructs a prior distribution of models at each location defined by allowed perturbations relative to the reference model as well as model constraints. The principal output is the posterior distribution of models that satisfy the receiver function and surface wave data (Rayleigh phase and group speeds and H/V) within tolerances that depend on data uncertainties. The statistical properties of the posterior distribution quantify aspects of model error as discussed later in the paper.

The Bayesian nature of the inversion refers to the fact that we sample model space to construct explicitly both the prior and posterior model distributions and that the relationship between these distributions is mediated by the likelihood function and governed by Bayes' theorem. Let $\pi(\mathbf{m})$ be the prior distribution of models and $P(\mathbf{m})$ be the posterior distribution. Bayes' theorem tells us that

$$P(\mathbf{m}) = k\, L(\mathbf{m})\, \pi(\mathbf{m}), \tag{3}$$

where k is a normalization constant (which does not affect the shape of the posterior distribution) and $L(\mathbf{m})$ is the likelihood function, which is a measure of the degree of fit to the data by the model $\mathbf{m}$ as follows:

$$L(\mathbf{m}) = \exp(-S(\mathbf{m})), \tag{4}$$

$$S(\mathbf{m}) = \sum_{i=1}^{N} \frac{\left(d_i - d_i^{\mathrm{pred}}\right)^2}{2\sigma_i^2}. \tag{5}$$

Here d_i is an observation with uncertainty σ_i, d_i^{pred} is the predicted datum from model $\mathbf{m}$, and N is the number of observations. *Shen et al.* [2013b] modified the likelihood function by introducing an additional weight to discriminate between the dispersion measurements and receiver functions in the likelihood function (further downweighting the receiver functions), but that is not done here. The only data weights are the estimated measurement errors.

The posterior distribution reflects both the prior constraints and the data used in the inversion. The Monte Carlo nature of the inversion refers to the fact that the search of model space is a stochastic process in which Markov chains of models are governed by a transition probability that depends on the fit to the data. The transition probability we use is the Metropolis law, as described by *Shen et al.* [2013b]. For each station we retain on average about 8500 models in the posterior distribution. Most of these models are not statistically independent of one another, and we discuss the impact of this fact on our interpretation of the posterior distribution in section 4.2.

Examples of marginal prior and posterior distributions for particular model characteristics are shown for two stations in Figure 7, in which there is an explicit comparison between results using surface wave dispersion alone (SW) and using all three data sets (All Data: surface wave disperion, receiver functions, and H/V measurement). The prior distribution is represented with the gray histograms, the posterior distribution based on Rayleigh wave dispersion alone is presented as the black-outlined white histograms, and the posterior distribution based on all three data sets is shown with the red histogram. As seen in Figure 3a, because of a clear Moho P-to-S conversion in the receiver function at station Z21A (Winston, NM), the joint inversion better constrains lower crustal V_s and crustal thickness (Figures 7b and 7c). Surface wave data alone do not constrain either crustal thickness or the jump in V_s across Moho at this station well. As seen in Figure 3c (C23A, Lambert, MT), the receiver function and H/V ratio are characteristic of thick sediments, and the joint inversion

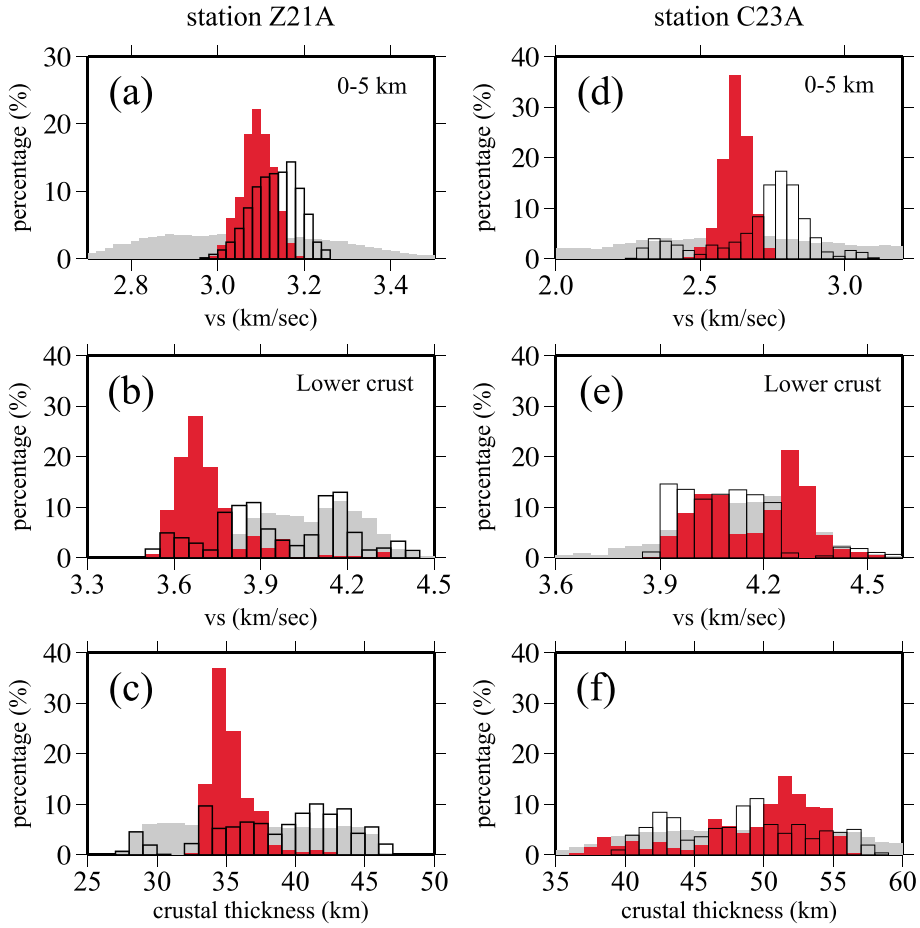

Figure 7. Example comparison of prior and posterior marginal distributions in the Bayesian Monte Carlo inversion for three model characteristics at two stations: (a–c) Z21A (Winston, NM) and (d–f) C23A (Lambert, MT). Gray histograms are the prior distribution; white histograms are the posterior distribution using surface wave dispersion data alone (Rayleigh wave group and phase speed measurements); and red histograms are the posterior distributions for the joint inversion of surface wave dispersion data, receiver functions, and Rayleigh wave *H*/*V* measurements at each station. (top row) Shear wave speed averaged between 0 and 5 km depth, (middle row) shear wave speed directly above the Moho, and (bottom row) crustal thickness (local elevation + depth of Moho below the geoid). If the red distribution is narrower and more peaked than the white distribution, then data other than surface wave dispersion constrain that model variable. For example, the receiver function at station Z21A (Figure 3a) improves the crustal thickness estimate but not at station C23A where surface sediments obscure the Moho phase conversion in the receiver function (Figure 3c).

better constrains shallow crustal structure than the inversion with surface wave dispersion alone (Figure 7d). Because reverberations in the receiver function obscure a possible Moho *P*-to-*S* conversion in the receiver function, the joint inversion does not, however, constrain lower crustal structure or crustal thickness appreciably better than the surface wave dispersion data alone (Figures 7e and 7f). The details of the inversion at each station depend on the nature of the receiver function and *H*/*V* measurements, but on average the vertical discontinuity structure of the crust is clarified, and the vertical resolution of the model is improved by introducing these data into the inversion with surface wave dispersion data. This is discussed futher in section 4.3 below.

We present examples of resulting models at a variety of locations in Figure 8. Each model is presented beneath a single station and corresponds to the data presented in Figure 3. At each depth the width of the full posterior distribution is shown, as are the mean and standard deviation of the posterior distribution which we use to summarize the 3-D model.

3.3. Fit to the Data

There are fairly strong constraints imposed in the inversion, including the smoothness of the model between discontinuities; the monotonic increase of shear wave speeds with depth in the crust; particular relationships

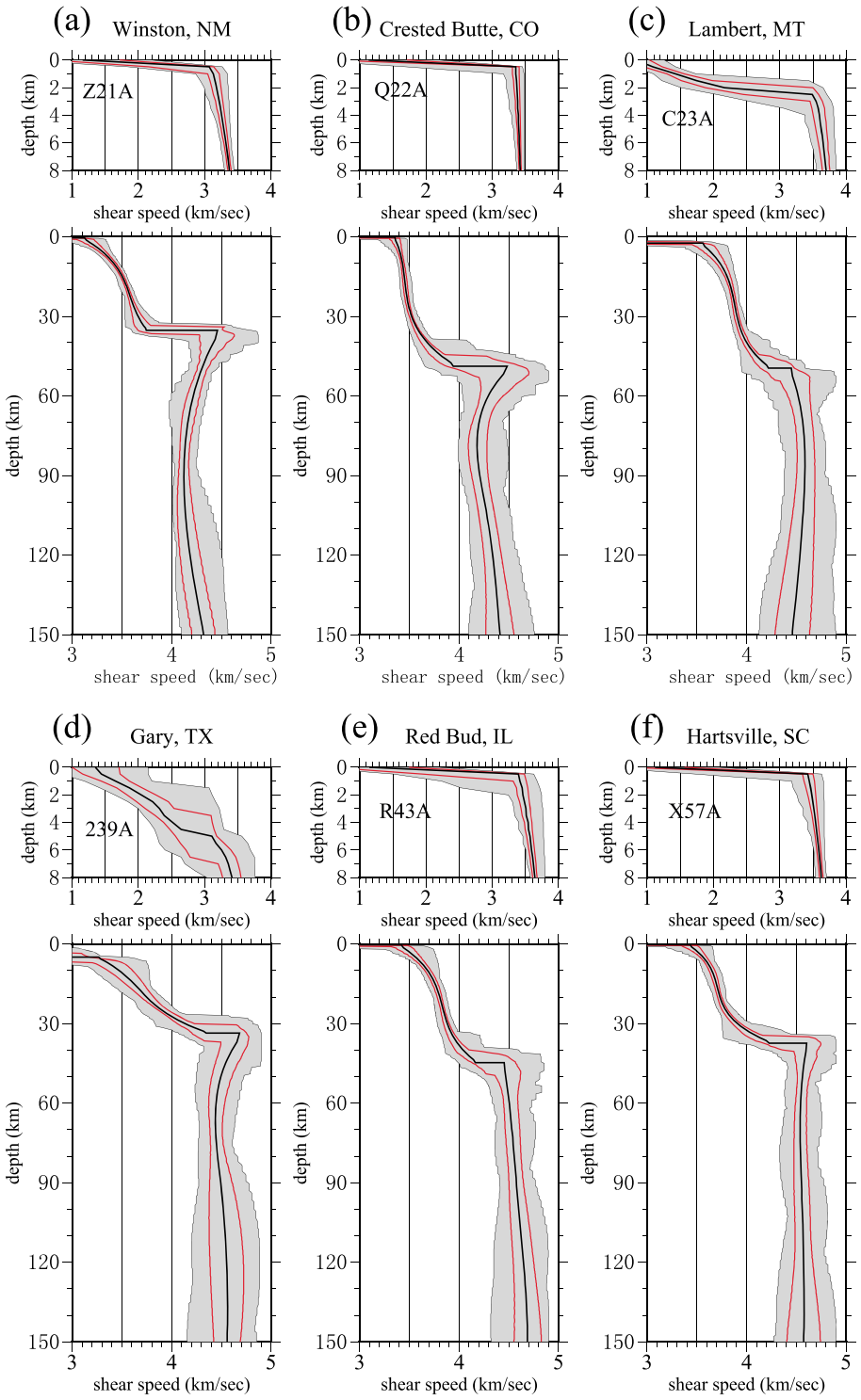

Figure 8. Examples of the depth dependence of the width of the posterior distribution from the joint inversion of all data at the six locations identified with red stars in Figure 1. The full width of the posterior distribution for shear wave speed is shown with the gray shaded corridor. The mean of the distribution is identified with a solid black line, and the 1 standard deviation contours are shown with red lines. For each location, the model is presented in two plots: (top) the model to 8 km depth in order to highlight sedimentary structure (shear velocity and thickness) and (bottom) the model to 150 km depth. The standard deviation of the posterior distribution is largest near the Moho and below 120 km depth.

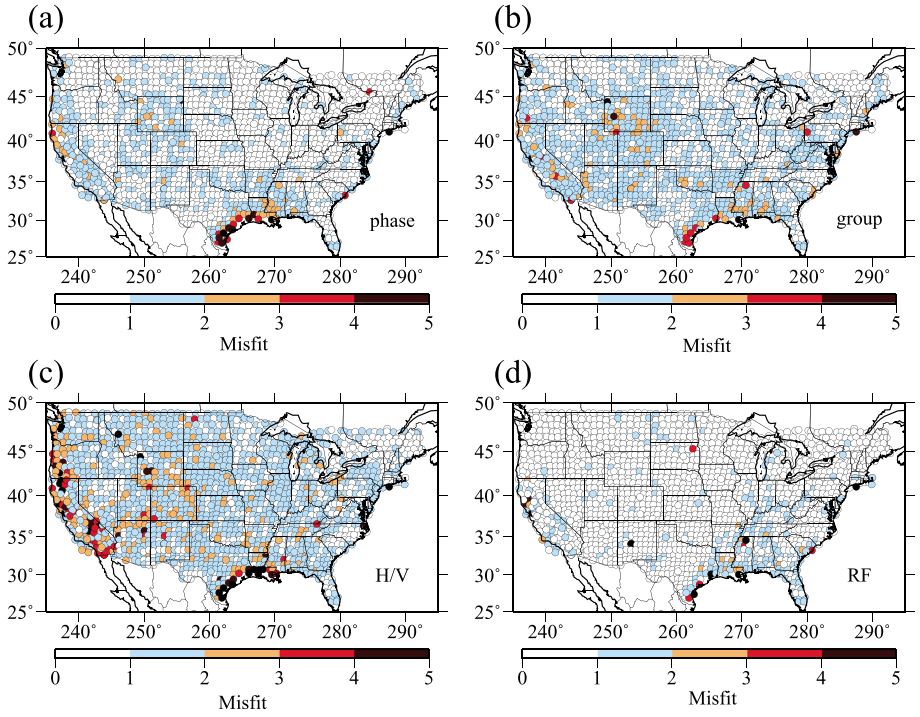

Figure 9. Geographic variation in the fit to the data by the best fitting model that results from the joint inversion of all data, presented at each station. Fit to (a) Rayleigh wave phase speed data averaged from 8 to 90 s period, (b) Rayleigh wave group speed data averaged from 8 to 40 s period, (c) Rayleigh wave *H/V* measurements averaged from 20 to 90 s period, and (d) receiver function data averaged from 0 to 10 s after the arrival of the *P* wave. Fits are defined as the square root of the reduced χ^2 misfit (equation (6)).

between V_s, V_p, and ρ as a function of depth; and a specified range of values considered for each model variable (Table 3). These constraints are imposed to reduce the model space searched and make the Monte Carlo search more efficient, but we view them as hypotheses which are tested in the inversion. The first question we have is whether the model is sufficiently flexible to allow the data to be fit across the entire region of study. If the data can be fit subject to the constraints, then extending the model beyond the constraints is not substantiated by the data alone. There may be good reasons to believe that the Earth does not satisfy the particular constraints imposed here, but if the data are fit subject to the constraints, this issue needs to be taken up in the construction of the prior distribution.

Figure 9 presents a summary of data fit in the joint inversion of all three data types, in which the square root of reduced chi-square is shown for Rayleigh wave phase speed, Rayleigh wave group speed, Rayleigh wave *H/V* measurements, and receiver functions. We refer to the square root of reduced chi-square misfit as "reduced χ misfit," which is defined as follows:

$$\chi_{\mathrm{red}} = \sqrt{\chi^2_{\mathrm{red}}} = \left(\frac{2}{N} S(m)\right)^{1/2}, \tag{6}$$

where $S(\mathbf{m})$ is the misfit function defined for model **m** by equation (5) and N is the number of observations. Misfit to the Rayleigh wave data (Figures 9a–9c) is averaged over period, and misfit to the azimuthally independent receiver functions is averaged over time (from 0 to 10 s). A χ_{red} of unity means that the data are fit on average at the level of 1σ, where σ represents data error, a value of 2 implies that the data are fit on average at the level of 2σ, and so forth.

On average, Rayleigh wave phase and group speeds are fit to better than 2σ (Figures 9a and 9b). Exceptions occur in regions of thick sediments where short-period group speeds are particularly sensitive, e.g., the Mississippi Embayment and Gulf Coast, the Green River basin of southwestern Wyoming, and the Central Valley of California. In these regions, greater flexibility in the construction of the sedimentary model is probably required, perhaps to include a larger range and perhaps different depth variation of the V_p/V_s ratio and

relaxation of the constraint on the monotonic increase of V_s with depth in the basin. *H/V* is also fit on average to better than 2σ (Figure 9c), but there are more regions where the data are fit poorly. Again, most of these are in sedimentary basins and *H/V* is strongly sensitive to sedimentary structure. The overall higher level of misfit for *H/V* illustrates that this datum tends to compete with short-period group speeds in the inversion. These two data types can be reconciled on average, but greater model flexibility is probably needed in several locations across the U.S. We have chosen not to allow this greater flexibility here, choosing instead a single parameterization across the U.S. for simplicity. The model presented in this paper is not intended to be the last word on structure across the U.S. As Figure 9d shows, receiver functions are typically fit to better than 1σ across the U.S. There are exceptional stations where azimuthally independent receiver functions cannot be well fit jointly with the other data in the inversion, but they are rare. The exceptional fit to the receiver functions may mean that we have somewhat overestimated the uncertainties in the receiver functions. The effect is that we do not attempt to fit small wiggles in the azimuthally independent receiver functions.

4. Results

At each location and for each depth, we summarize the posterior distribution of models with its mean ($\overline{m}$) and standard deviation (σ_m). Examples of the mean and standard deviation of the posterior distribution can be read off the vertical profiles shown in Figure 8. The addition of different data into the inversion makes the posterior distributions increasingly Gaussian in character. This effect can be seen clearly in the marginal distributions presented in Figure 7. For example, at station Z21A (Figures 7a–7c), the prior distributions are approximately uniform for all three model variables. For the inversion using surface wave data alone, the posterior distribution is strongly bimodal in the lower crust and fairly uniform for crustal thickness. However, when receiver functions and *H/V* measurements are added to the inversion, the posterior distributions are much more Gaussian in shape and not multimodal. This is also true for stations C23A in the shallow crust (Figure 7d) where the introduction of *H/V* measurements strongly has affected the posterior distribution. However, the posterior distribution in the lower crust and for crustal thickness is bimodal or multimodal (Figures 7e and 7f) because sedimentary reverberations in the receiver function at this location obscure constraints on crustal thickness. At most locations and for most model characteristics across the U.S., the mean and standard deviation provide reliable summaries of the posterior distribution except in a small minority of cases when lower crustal and Moho distributions may bifurcate. Thus, in the following, we summarize the model in terms of these statistics ($\overline{m}$ and σ_m) but retain the caveat that in some locations (particularly in sedimentary basins), the posterior distribution may possess complications not captured by the mean and standard deviation. To define the final 3-D model, we follow *Shen et al.* [2013a, 2013b] and apply simple kriging to interpolate the depth-dependent quantities ($\overline{m}$ and σ_m) onto a 0.25°×0.25° grid and construct a uniform model of the crust and uppermost mantle to a depth of 150 km across the U.S.

4.1. Regionally Averaged Models and Variations Within Each Region

Before turning to discuss the subregional-scale variations in the 3-D model, we first seek to assess large-scale averages and variations in the model. To do this we divide the contiguous U.S. into three regions, identified in Figure 10a as the western region, the continental core region, and the eastern region. The eastern region also encompasses much of the south and is perhaps best viewed as the margin of the continent that has been tectonically modified with influence from the south and east. Figure 10b presents the three regional averages computed from the mean of the posterior distribution at each station across each region. At each location we stretch or compress the crustal model vertically to match the average crustal thickness in the region before computing the regional average. Similarly, depth in the mantle is taken relative to Moho depth which we then normalize to the Moho depth averaged across the region. Not surprisingly, the recently tectonically deformed western region is distinct, with considerably slower crust and mantle and thinner crust than the other regions. The eastern region is also somewhat slower than the core region with a thinner crust.

Spatial variations across each of the three regions are shown in Figure 10c, in which the standard deviation relative to the regional mean is presented at each depth. Spatial variability is greatest near the surface, which is caused predominantly by variations between locations with and without sediments. Due to the exceptionally thick sediments in the Mississippi Embayment, the greatest shallow variability lies in the eastern region. In the middle crust, the western region is considerably more variable (~3%) than the other regions, being approximately twice as variable as in the core region (~1.5%). Variability peaks up near the Moho due to

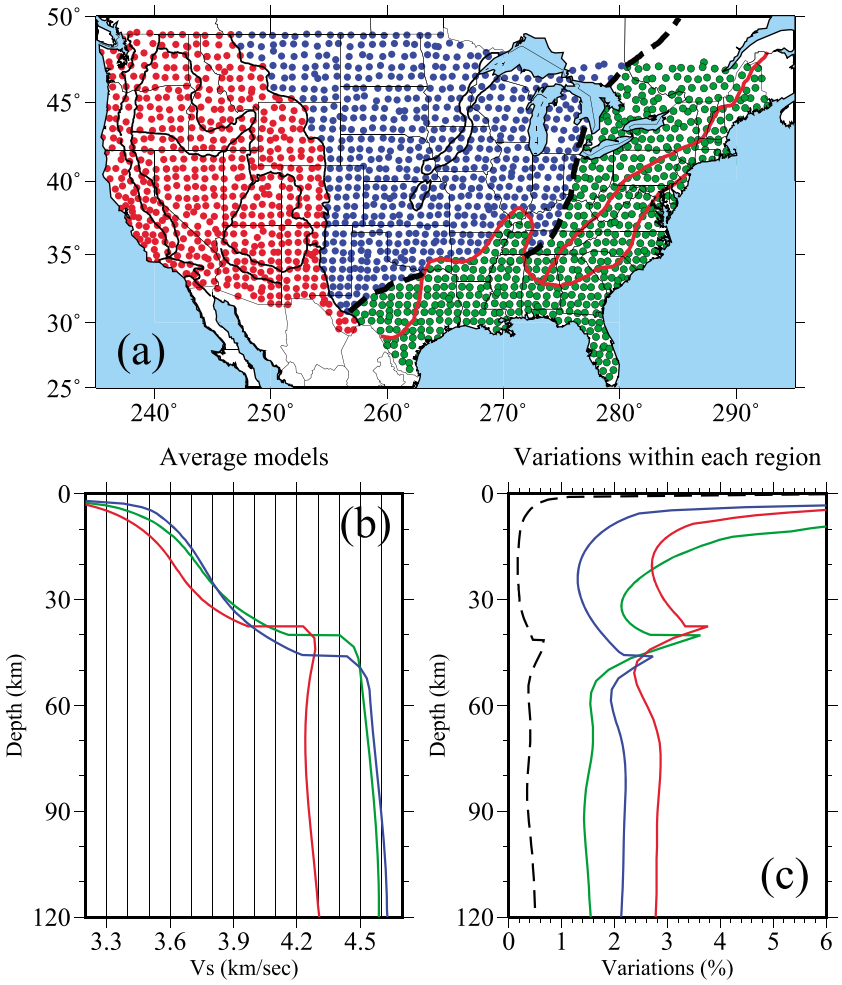

Figure 10. (a) The definition of the three regions in which regional averages and variability are computed: (red circles) "Western Region" west of the Rocky Mountain front, (blue circles) "Continental Core Region" between the Rocky Mountain front and the Grenville front (dashed line), and (green circles) the "Eastern Region" east and south of the Grenville front. (b) Shear wave speed as a function of depth averaged within each of the regions, color coded in accordance with the regional colors in Figure 10a. (c) Spatial variations in shear wave speeds across each region presented with colors as in Figure 10b, defined as the standard deviation around the mean at each depth. The dashed black line is the estimate of the standard deviation in the mean of the posterior distribution ($\sigma_{\overline{m}}$) averaged across the U.S., which we interpret as the average model error due to random processes.

lateral variations in Moho structure; some locations have a gradient Moho, and others have a sharp Moho. These variations have a greater imprint on uppermost mantle structure than on lower crustal structure and decay quickly with depth in the mantle. In the mantle, regional variations lie between 1.5% (eastern region) and 3% (western region). The core region has larger geographical variations in the mantle than the eastern region due to heterogeneity beneath the western Great Plains, which appears to be affected by orogens that lie largely in the western region and affect crustal structure only in the western region. Mantle heterogeneity in the core region, which is about 2%, is actually larger than midcrustal heterogeneity in that region (~1.5%).

4.2. Assessing Model Error: Differentiating Between Nonsystematic and Systematic Errors

In order to interpret the spatial variations observed in the means of the posterior distributions, it is necessary to compare them with estimates of model uncertainties. What we have estimated at every location is the posterior distribution of models $\{m_i\}$ that satisfy the data at the point. Here let us consider m_i to represent a model characteristic, say for example, V_s at a particular depth. We summarize the set $\{m_i\}$ with its mean, $\overline{m}$, and standard deviation, σ_m. We use $\overline{m}$ as the estimate of the model at each location. The question we consider here is what is the best estimate for the error or uncertainty in our estimated model at this location?

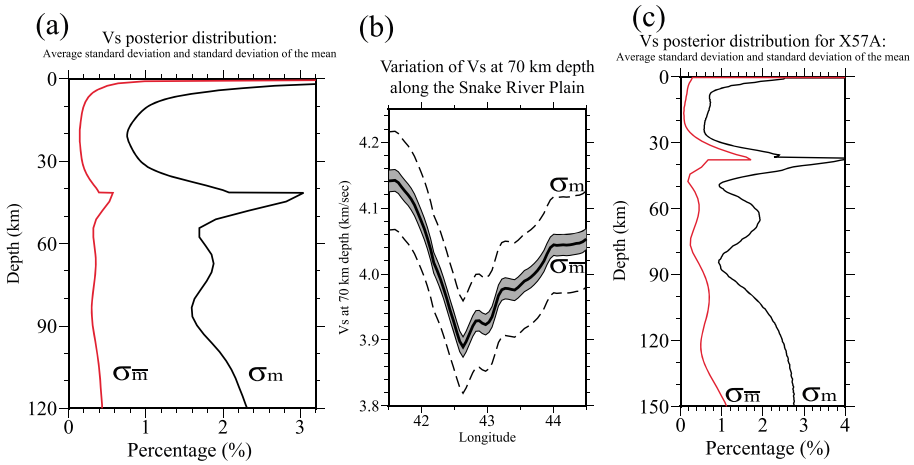

Figure 11. (a) Black line is the standard deviation of the posterior distribution (σ_m) averaged across the entire U.S. Red line is the estimate of the standard deviation of the mean ($\sigma_{\overline{m}}$) of the posterior distribution averaged across the U.S. (computed by scaling σ_m by 0.2), which we interpret as the average model error due to random processes (same as dashed line in Figure 10c). (b) Variation in V_s (solid black line is the mean of the posterior distribution) along the Snake River Plain (profile X_2; Figure 22). Dashed lines mark ±1 σ_m, and the gray corridor marks ±1 $\sigma_{\overline{m}}$. (c) Comparison of (black line) σ_m and (red line) $\sigma_{\overline{m}}$ for the inversion at station X57A (Hartsville, SC). $\sigma_{\overline{m}}$ is computed by brute force in which numerous posterior distributions are computed at this station and the standard deviation of the means of the posterior distributions is computed from them.

By "error," we mean the way our model deviates from the Earth, where our model is $\overline{m}$. We will gloss over how we define "Earth" here and assert the following: model error $= e_{\overline{m}} = \overline{m} - m_{\oplus}$, where $m_{\oplus}$ is the property of the Earth that the model variables m_i represents. If we let the notation $<>$ represent an estimated value, then we seek the estimated error in $\overline{m}$ or $<e_{\overline{m}}>$. One candidate for the model error estimate is the standard deviation of the posterior distribution, σ_m. The first thing we do here is eliminate σ_m as a candidate for $<e_{\overline{m}}>$.

4.2.1. Inadequacy of the Standard Deviation of the Posterior Distribution to Represent Model Error

The average of σ_m across the contiguous U.S. as a function of depth is shown with the solid black line in Figure 11a. Average values for σ_m are about 1.5% in the crust, although they dip appreciably in the middle crust and are somewhat larger in the mantle (~1.8% on average). These values peak near the free surface and Moho due to trade-offs between internal structures and boundary topography.

A great many factors affect the standard deviation of the posterior distribution, σ_m. Posterior distributions are affected by uncertainties in the data, which control which models are accepted to form the distributions, but they are also affected strongly by trade-offs between model variables at different depths. Vertical model oscillations are particularly troublesome and important and are often nonphysical. In defining the prior distribution, we have attempted to limit such oscillations and trade-offs by introducing vertically smooth basis functions as well as model constraints (positive jump across discontinuities, maximum velocity in each layer, and monotonic increase of shear wave speed in the crust). Nevertheless, the spread of the posterior distribution still reflects such effects and, as a consequence, strongly reflects the model prior. Indeed, relaxing the prior constraints produces more vertically oscillatory models, which produces a larger standard deviation in the posterior distribution, but it has a much smaller impact on the mean of the distribution. For this reason, the standard deviation of the posterior distribution σ_m is not a good estimate of fluctuations in the mean of the posterior distribution.

The inadequacy of σ_m to measure model uncertainty can be seen further by comparing the spatially averaged σ_m, shown with a solid black line in Figure 11a, with the spatial variations within each of the three regions, shown in Figure 10c. The spatially averaged σ_m is about the same size as the variations within each region. If σ_m were used as the estimate of model uncertainty, then the interpretation of structural variations within regions may be questionable. The geological coherence of the model and the stability of the posterior distributions, however, imply that σ_m is an overly conservative estimate of model uncertainty, albeit one that captures an estimate of the relative reliability of the resulting model. An example of this is shown in Figure 11b, which illustrates that the mean of the posterior distribution at 70 km depth in the mantle changes smoothly along the Snake River Plain and fluctuates at a level much smaller than σ_m.

In summary, σ_m does not provide a good absolute estimate of the error in the estimated model $\overline{m}$. Rather, it is actually an estimate of the error in each of the constituent models in the posterior distribution, $\{m_i\}$. The averaging process to compute $\overline{m}$ beats down random errors as discussed in section 4.2.2.

4.2.2. Nonsystematic Error: The Standard Deviation of the Mean of the Posterior Distribution

We seek a more useful estimate of model uncertainty than σ_m. In doing so we would like to discriminate between nonsystematic model fluctuations, which we interpret as model errors caused by observational errors and trade-offs between model parameters, from systematic errors caused by choices made in the construction of the prior distribution, including such things as model parameterization, the extent of the model space searched, and constraints imposed in the inversion. The estimated model, $<\overline{m}>$, will be a combination of the real Earth, $m_\oplus$, and the estimated error, $<e_{\overline{m}}>$, as follows:

$$< \overline{m} >= m_\oplus + < e_{\overline{m}} >= m_\oplus + < e_{\text{sys}} + e_{\text{data}} + e_{\text{null}} >= m_\oplus + < e_{\text{sys}} > + < e_{\text{nonsys}} > . \quad (7)$$

We consider the model error to arise from two components, a systematic (e_{sys}) and a nonsystematic (e_{nonsys}) contribution. We also refer to nonsystematic error as random error or e_{ran}. The nonsystematic contribution to model error arises from errors in the data, e_{data}, and model errors caused by trade-offs between variables that define the model, which we refer to as e_{null}. The last equality in equation (7) follows from the assumed independence between the systematic errors, which are caused locally by the deviation of the Earth from our assumptions and constraints, and the nonsystematic errors caused by data errors and trade-offs.

Here we discuss our attempt to quantify nonsystematic or random error, which is much less problematic than estimating systematic error or model bias. Model bias is the subject of section 5.3.

Our approach is to equate nonsystematic or random error with model fluctuations, which are inversely related to the stability of the mean of the posterior distribution. The aim is for our assessment of random error to reflect the fluctuations observed in the model, such as those seen in Figure 11b along the Snake River Plain. We posit that the standard deviation of the mean of the posterior distribution, $\sigma_{\overline{m}}$, provides a reasonable estimate of the stability of the mean of the model or the random error in the model, $<e_{\text{nonsys}}>$. The standard deviation of the mean of the model, $\sigma_{\overline{m}}$, contrasts with the standard deviation of the posterior distribution, σ_m, as follows:

$$\sigma_m^2 = \frac{1}{N_m}\sum_{i=1}^{N}(m_i - \overline{m})^2, \quad (8)$$

$$\sigma_{\overline{m}}^2 \approx \frac{1}{N_I}\sigma_m^2, \quad (9)$$

where N_m is the number of models in the posterior distribution and N_I is the number of independent models in the posterior distribution. As discussed further below, N_I is typically unknown but it definitely much smaller than N_m.

One method to estimate $\sigma_{\overline{m}}$ (and hence $<e_{\text{nonsys}}>$) is to scale the standard deviation of the posterior distribution (σ_m) by the inverse square root of the number of independent models in the distribution as suggested by equation (9). We describe how we estimate the number of independent models, N_I, in the next paragraph, but when we apply the scaling we obtain an average $\sigma_{\overline{m}}$ across the U.S. shown with a dashed line in Figure 10c and a red line in Figure 11a. We estimate that $\sigma_{\overline{m}}$ on average in the central crust is about 0.2% and in the mantle at about 100 km depth it is about 0.4% except directly beneath Moho. These values are considerably smaller than the variations we observe within the three regions of Figure 10 and fairly represent our degree of belief in the model characteristics. The variations in structure within the regions are the subject of sections 4.3, 4.4, 5.1, and 5.2.

The standard deviation of the mean of the posterior distribution, $\sigma_{\overline{m}}$, which we identify with the random model error, is determined from the mean of the posterior distribution here by dividing by a number between 4 and 5: $\sigma_{\overline{m}} \approx \sigma_m/4$. We arrive at this range by determining that the number of independent models in the posterior distribution is 0.2%–0.3% of the models in the distribution. The average number of models in the posterior distribution, N_m, is about 8500; thus, the number of independent models N_I lies between 16 and 25 models, on average. Applying the square root we get a scaling factor of 4 or 5 in the standard deviation.

4.2.3. Computing the Standard Deviation of the Mean of the Posterior Distribution

The procedure we use to determine the number of independent models is based on the discussion of *Mosegaard and Tarantola* [1995], who present a method based on analyzing the likelihood function within

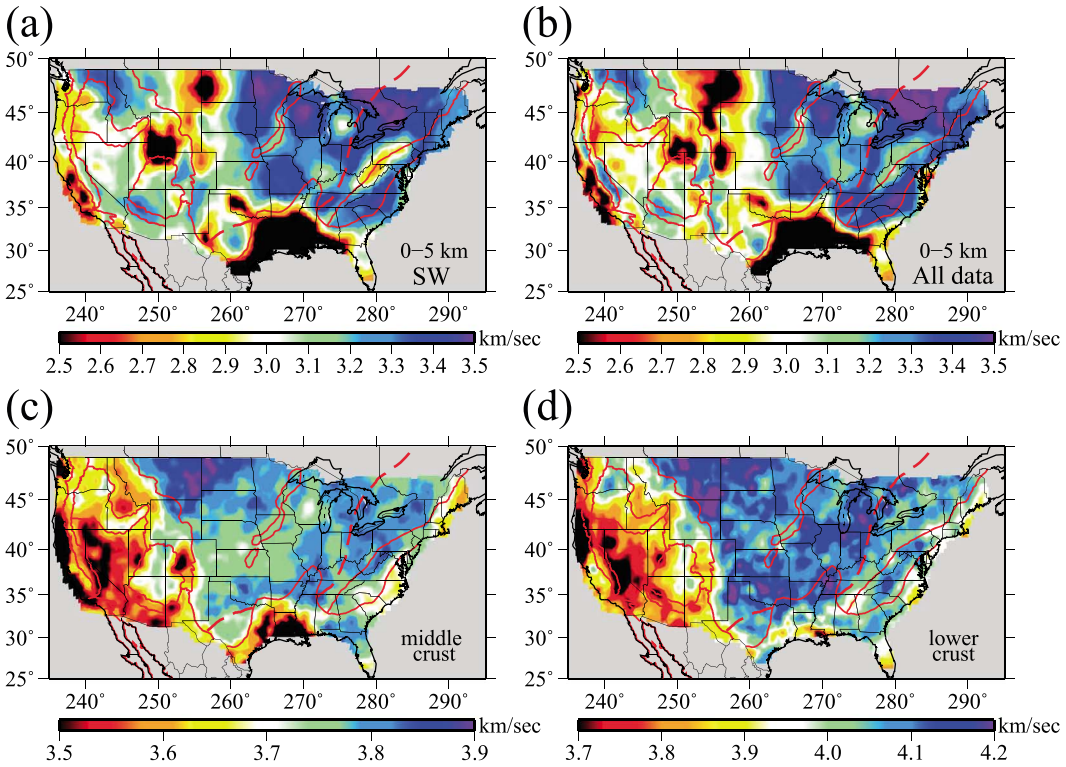

Figure 12. Various crustal features. (a) Mean of the posterior distribution of the average shear wave speed averaged in the top 5 km below the free surface using surface wave dispersion measurements alone. (b) Same as in Figure 12a, but the inversion uses all data (including receiver functions and Rayleigh wave *H/V* measurements). Shallow structure is modified predominantly by the introduction of the *H/V* data. (c) Mean of the posterior distribution of the shear wave speed in the middle crust averaged within 4 km of the midpoint between the free surface and Moho, taken from the inversion using all data. (c) Mean of the posterior distribution of the shear wave speed in the lower crust averaged within 3 km of Moho in the crust, taken from the inversion using all data.

the equilibrium part of each Markov chain. Let $\{m_i\}$ be an ordered set of models that compose the equilibrium part of a Markov chain sampling of model space. Typically, the likelihood function increases in magnitude as the Markov chain progresses from the initial or seed model and then plateaus [e.g., *Shen et al.*, 2013b, Figure 8] where it oscillates. The equilibrium part of the Markov chain is the plateau region. Now consider the discrete function $L(m_i)$, which is the likelihood as a function of model number within the equilibrium region of the Markov chain. *Mosegaard and Tarantola* [1995] suggest computing the autocorrelation of $L(m_i)$, such that the number of models that are required for the autocorrelation to return to 0 is the number of models needed to reestablish statistical independence. Given our sampling algorithm, we find that the Markov chain has to march through between 300 and 500 accepted models before it achieves independence relative to its starting state. Thus, only approximately 1 in 300 to 500 models in the posterior distribution is independent. This means that, on average, N_l lies between 16 and 25 so that the local standard deviation of the distribution should be divided by between 4 and 5 to estimate the standard deviation in the mean of the distribution, $\sigma_{\overline{m}}$, which we equate with $<e_{\mathrm{nonsys}}>$.

As a consistency test of this estimate of the standard deviation of the mean of the posterior distribution, $\sigma_{\overline{m}}$, we have performed several brute force calculations of the standard deviation of the mean for a number of stations by rerunning the Bayesian Monte Carlo inversions many times. This allows us to construct a set of different posterior distributions from which we can compute the standard deviation of the mean across these distributions. The results for station X57A (Hartsville, SC) are shown in Figure 11c, which compares the standard deviation of the mean with the original standard deviation of the posterior distribution at this point. On average, from 5 to 150 km depth, the standard deviation of the mean, $\sigma_{\overline{m}}$, is about 25% of the standard deviation of the posterior distribution, σ_m. This result is consistent with the scaling analysis based on the likelihood function but is numerically much more expensive to compute. We obtain similar but not identical results at other stations.

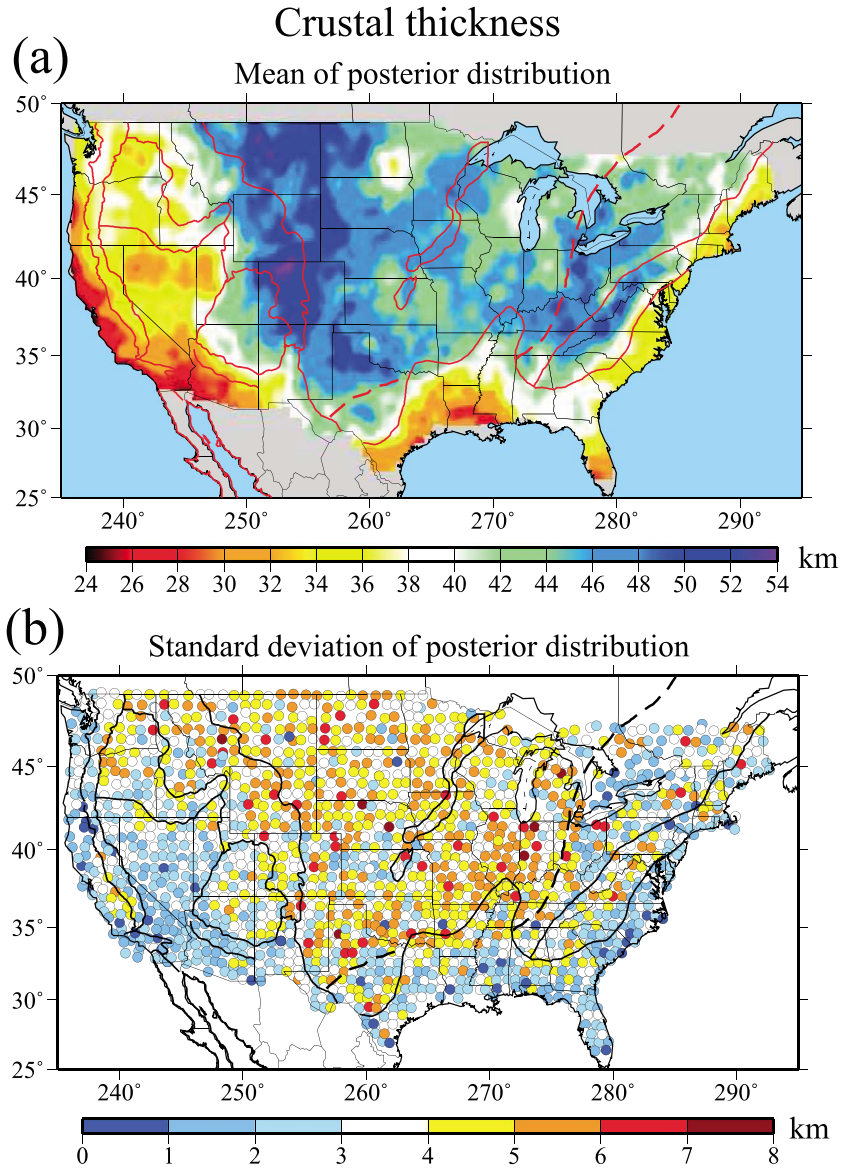

Figure 13. Crustal thickness. (a) Mean of the posterior distribution of crustal thickness (distance from the free surface to Moho) taken from the inversion using all data. (b) Standard deviation of the posterior distribution (σ_m) of crustal thickness from the inversion using all data.

4.2.4. Discussing Model Error

In the rest of the paper and in all figures, when summarizing the posterior distribution we will present the standard deviation of the posterior distribution, σ_m, which provides a reasonable relative error estimate. To estimate the random or nonsystematic error in order to quantify the stability of the model, however, one should divide these values by 4–5 to get a better estimate of the standard deviation of the mean, $\sigma_{\overline{m}}$. The standard deviation of the mean not only includes the effect of measurement errors but also the effects of covariances between model variables and, therefore, remains a fairly conservative estimate of model uncertainty caused by random errors. However, the standard deviation of the mean does not include the effect of systematic errors caused by erroneous assumptions and constraints imposed in the inversion. An assessment of the nature and potential magnitude of systematic error is presented in section 5.3.

4.3. Crustal Model

Horizontal slices of the mean of the posterior distribution for several depths in the crust are presented in Figure 12. Figures 12a and 12b illustrate the effect on estimated shallow structures of the inclusion of receiver

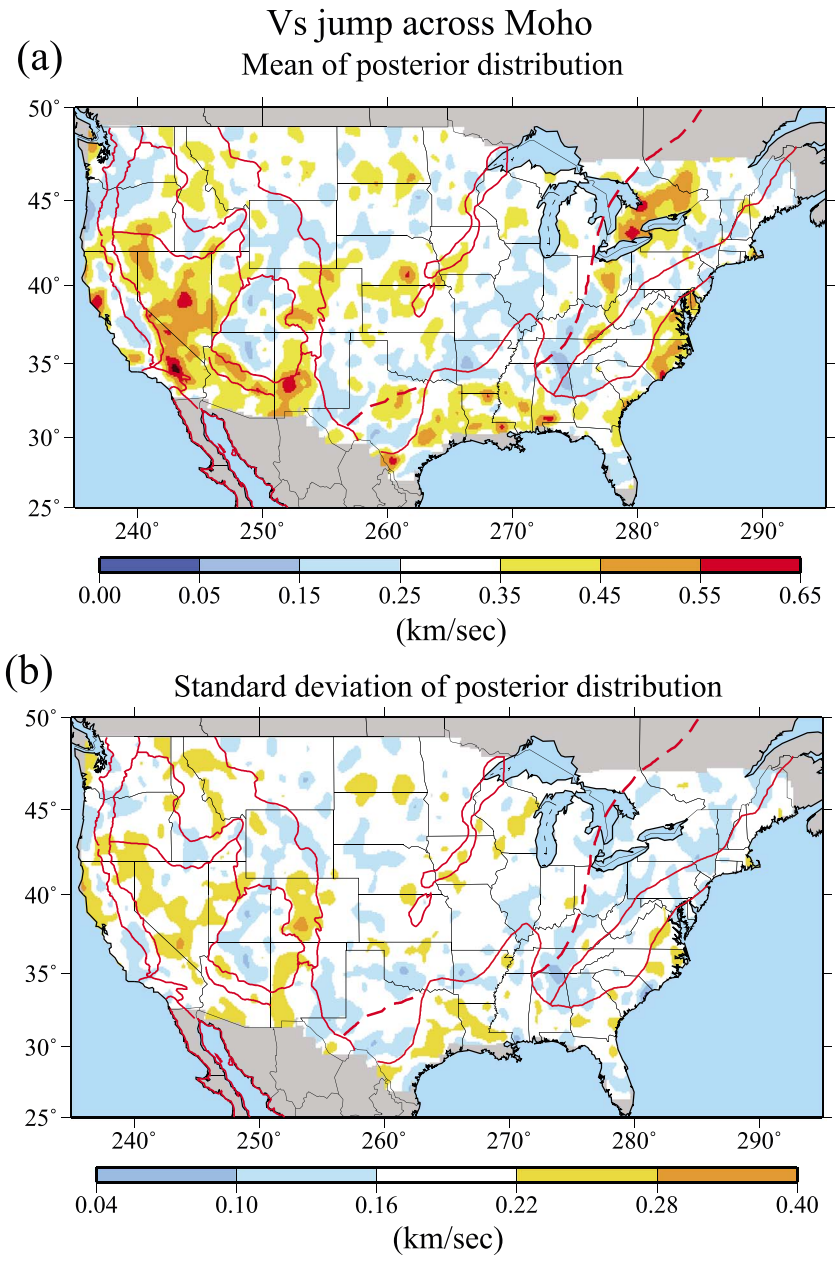

Figure 14. (a) The jump in V_s across Moho presented as the difference in V_s directly below and above Moho, taken from the mean of the posterior distribution at each depth and location. (b) The standard deviation of the difference between the shear wave speed below and above Moho computed using all models in the posterior distribution at each point.

functions and Rayleigh wave ellipticity measurements. Sedimentary basins dominate the structural variations in the top 5 km of the crust. The introduction of receiver functions and Rayleigh wave ellipticity measurements brings shallow structures, notably sedimentary basins, into sharper focus both laterally and vertically. This improves the crustal model, at least in the upper half of the crust.

There are a great many crustal features worthy of note and serious discussion, but this is beyond the scope of this paper. However, we note that there is stronger variation across the midcontinent in the middle crust than in the lower crust. We believe that the relatively low wave speeds (green anomalies) in the middle crust in Figure 12c across Nebraska, Kansas, Missouri, and Iowa are what *Chu and Helmberger* [2014] refer to as the "massive low-velocity zone in the lower crust." If so, it is in fact a midcrustal feature and although large in areal extent is only slow in a relative sense.

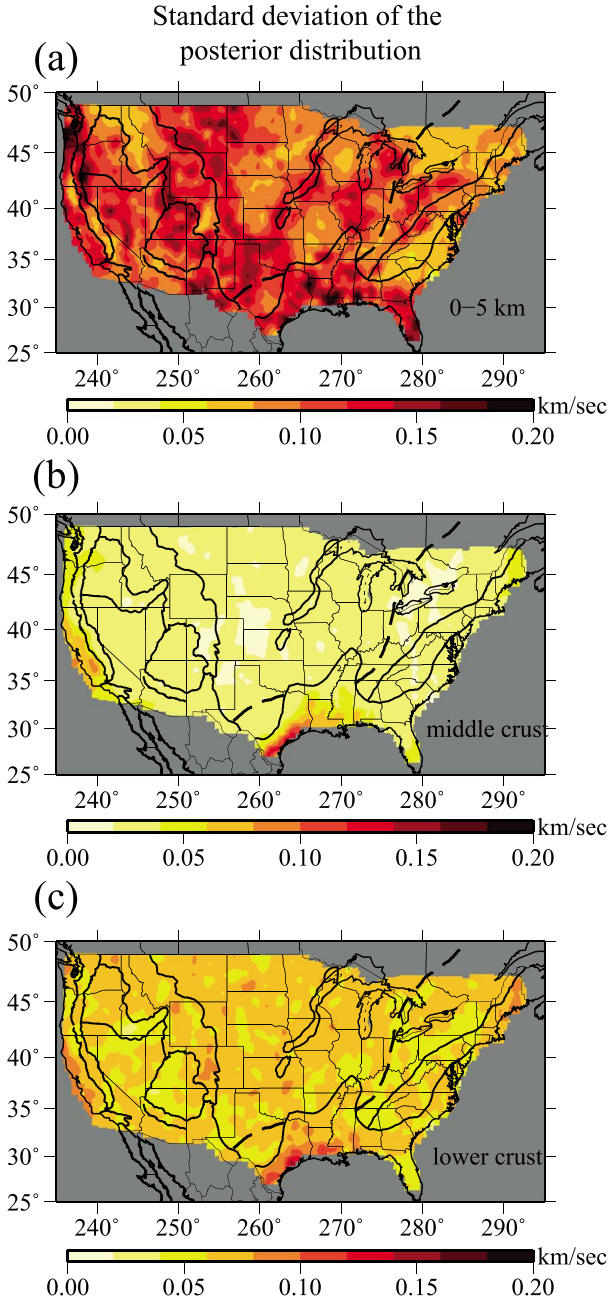

Figure 15. The standard deviation of the posterior distribution, σ_m, for V_s at different depths in the crust: (a) averaged over the top 5 km, (b) averaged in the middle crust within 4 km of the midpoint between the free surface and Moho, and (c) averaged in the lower crust within 3 km of Moho. In the crust, σ_m is largest near the free surface and Moho.

We note that the discussion in section 4.1 based on the regionalization of the U.S. into three regions was motivated by lower crustal structure, which is quite homogeneous across the core of the continent between the Rocky Mountain Front and the Grenville Front, which cuts across the south and eastern Midwest of the U.S.

The mean of the posterior distribution for crustal thickness is presented in Figure 13. The thickest crust lies under the Rocky Mountains in Colorado, and the thickest crust in the east is beneath the Appalachian Mountains. These results are not surprising, but there are many local variations in crustal thickness that deserve greater attention than we can pay them here, e.g., the very thin crust of eastern North Dakota, the thick crust extending from western New York through Kentucky in the region between the Grenville Front and the Appalachian Mountains, and the large region of relatively thick crust spanning the Mid-Continent Rift.

The mean of the posterior distribution of the vertical jump in V_s from the crust to the mantle is presented in Figure 14. On average V_s increases across the Moho from the crust to the mantle by about 300 m/s. However, there is substantial variation. For example, there are much larger jumps across the Moho in much of the Basin and Range Province and in southern Ontario between Lake Huron and Lakes Erie and Ontario. However, much smaller jumps produce a near gradient Moho, which is observed beneath the Colorado Plateau, in the Pacific Northwest overlying the subducting slab, beneath Illinois, and in other places distributed across the U.S.

The standard deviation of the posterior distribution of crustal velocities, crustal thicknesses, and the jumps in V_s across Moho are presented in Figures 13b, 14b, and 15. As discussed in section 4.2, to obtain an estimate of the standard deviation of the mean of the posterior distribution, which is a better representation of the random error in the model, one should divide the uncertainties shown in Figures 13b, 14b, and 15 by approximately 4–5.

Uncertainties in the V_s jump across Moho are presented in Figure 14b. Generally, uncertainties are largest where the jumps in V_s are largest, for example, the Basin and Range and the Colorado Rocky Mountains. Large jumps are usually imposed by the receiver functions, which do not provide precise constraints on the magnitude of the jump in V_s.

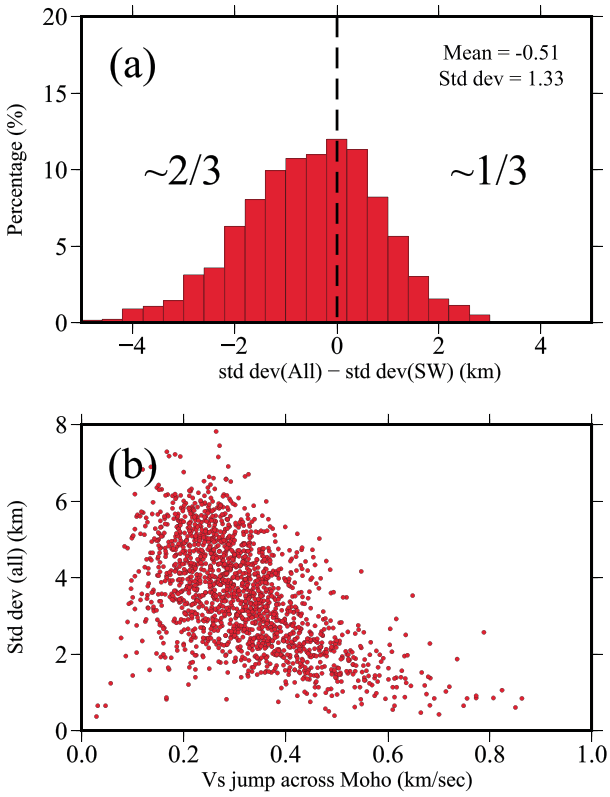

Figure 16. (a) Histogram of the difference between the local standard deviation of the posterior distribution (σ_m) of crustal thickness determined in the inversion using all data (Figure 13b), std dev (All), and the standard deviation based on surface wave data alone, std dev (SW), at the same location. (b) Plot of std dev (All) versus the jump across Moho (Figure 14a) at the same location.

Uncertainties in crustal velocities grow toward the top and bottom of the crust, as shown in Figure 11a and discussed already, and are quite laterally homogeneous across the U.S. (Figure 15). They are largest in the Mississippi Embayment due to the extremely thick sediments found there. The geographical pattern of uncertainties in crustal thickness correlates with crustal thickness, such that the larger uncertainties tend to be near the core of the continent. The depth of Moho for thicker crust is simply harder to determine than for thinner crust because the Airy phase in the group velocity curve, which reflects crustal thickness, migrates to longer periods and is more difficult to resolve clearly. The introduction of receiver functions in the inversion reduces the uncertainty in crustal thickness, on average. This is shown in Figure 16a. The inversion of surface wave dispersion together with receiver functions and Rayleigh wave ellipticity reduces uncertainty in Moho depth at about two thirds of the stations. At the other stations, however, the introduction of receiver functions in the inversion actually increases the uncertainty. In many cases this is because the receiver function reveals that the station is underlain by a gradient Moho or a complicated Moho structure such that crustal thickness is difficult to resolve. Indeed, the uncertainty in crustal thickness is strongly correlated with the jump in V_s across Moho as Figure 16b shows. A gradient Moho, characterized by a small jump at Moho, tends to produce large uncertainties in crustal thickness.

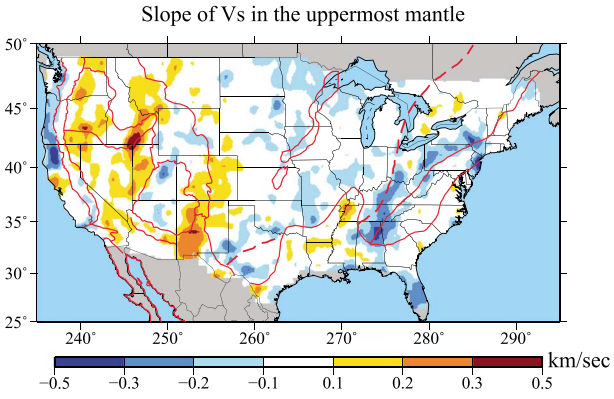

Figure 17. A low-velocity-zone (LVZ) in the shallow mantle? Plot of the difference between V_s at the top of the mantle directly below Moho and V_s 20 km below Moho, using the mean of the posterior distribution at each location. Warm colors indicate a negative vertical gradient indicative of a shallow LVZ, and cool colors indicate a positive vertical gradient in the uppermost mantle indicative of no LVZ.

4.4. Mantle Model

Uppermost mantle structure directly beneath the Moho varies strongly across the U.S. as shown in Figure 17. Across most of the U.S., the vertical slope of uppermost mantle V_s right beneath the Moho is essentially neutral; such that, V_s changes only minimally with depth. A vertical profile that provides an example of this is at Hartsville, SC, and is seen in Figure 8f. Such locations are colored white in Figure 17. At some locations, however, there is a strong negative slope with depth in the uppermost mantle, which typically indicates the existence of a low-velocity zone (LVZ) in the shallow mantle. Such locations are identified with warm colors in Figure 17 and are mainly confined to the western U.S. An example vertical profile is at Crested Butte,

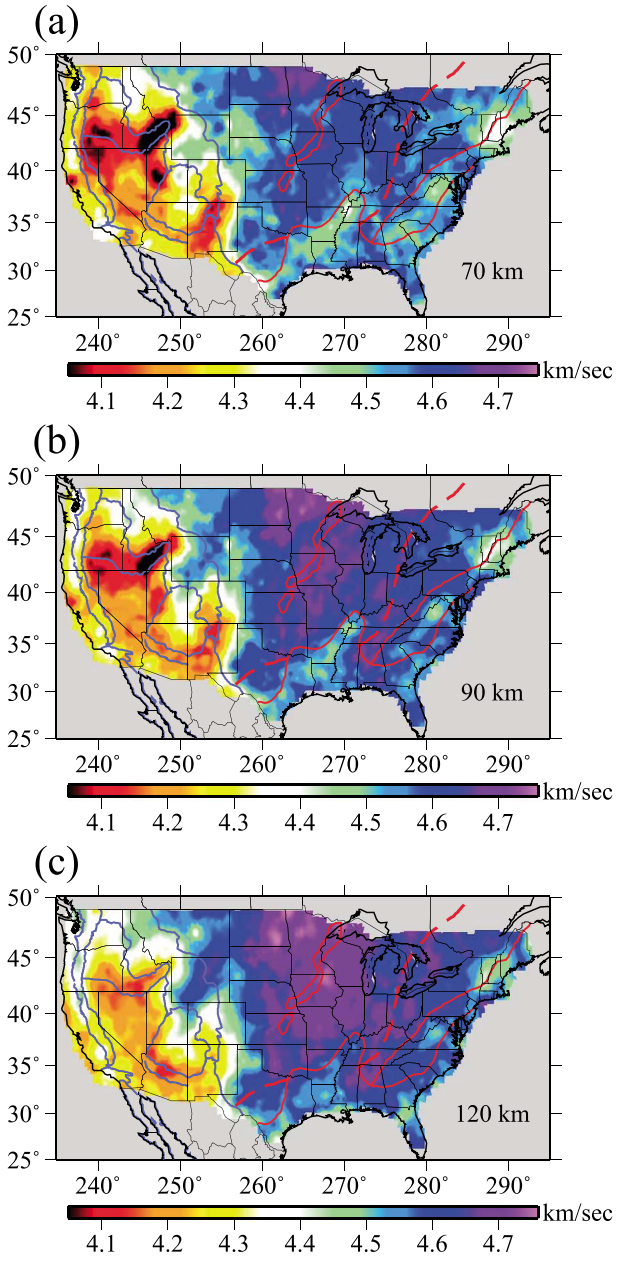

Figure 18. Mantle shear wave speeds at three depths, presented as the mean of the posterior distribution at each location: (a) 70 km depth, (b) 90 km depth, and (c) 120 km depth. V_S values are averaged vertically within 5 km of each stated depth.

CO, as can be seen in Figure 8b. In contrast, some locations have a positive slope with depth, meaning that there is no LVZ in the shallow mantle. Such locations are identified with cool colors in Figure 17 and are mainly found in the eastern U.S. An example vertical profile is at Red Bud, IL, as can be seen in Figure 8e. Typically, shallow mantle LVZs are found across much of the western U.S. outside the Wyoming Craton, the Colorado Plateau, and the Cascadia subduction zone. The strongest positive slopes in the uppermost mantle occur between the Grenville Front and the Appalachian Mountains, although weaker positive slopes also extend across large parts of the Midwest.

Several horizontal slices of V_S at depths of 70, 90, and 120 km in the upper mantle are presented in Figure 18. The most prominent contrast is the east-west dichotomy. Many of the structural features within the west (e.g., Snake River Plain and High Lava Plains low-velocity anomaly, rimming low-velocity anomalies around the Colorado Plateau and Wyoming Craton) are well known now, as they appeared in earlier studies that were prefaces to the current paper [e.g., *Moschetti et al.*, 2007, 2010a, 2010b; *Yang et al.*, 2008, 2011; *Bensen et al.*, 2009; *Lin et al.*, 2011; *Shen et al.*, 2013a, 2013b, 2013c]. Unlike low-velocity anomalies that typically attenuate with depth, the Wyoming Craton high-velocity anomaly increases in prominence with depth. The Cascadia slab is apparent at 120 km depth. The most prominent upper mantle anomaly in the east is the Reelfoot Rift [*Pollitz and Mooney*, 2014], which is predominantly a shallow low-velocity mantle anomaly. Relative low velocities in the uppermost mantle also underlie the Appalachian Mountains, the most prominent of which are found beneath New England and western Virginia.

The standard deviation of the posterior distribution in upper mantle shear wave speeds is presented in Figure 19. Again, as discussed earlier, to obtain a better estimate of the random error in the model, one should divide the uncertainties shown in Figure 19 by approximately 4–5. Uncertainties are fairly homogeneous with location across the U.S. but grow below 100 km depth as Figure 11a indicates.

5. Discussion

The features of the model are often most clearly discerned in vertical transects. Here we expand the discussion of model features by discussing four long east-west transects across the entire U.S. as well as three pairs of shorter vertical profiles situated in crossing patterns through notable features: the Snake River Plain,

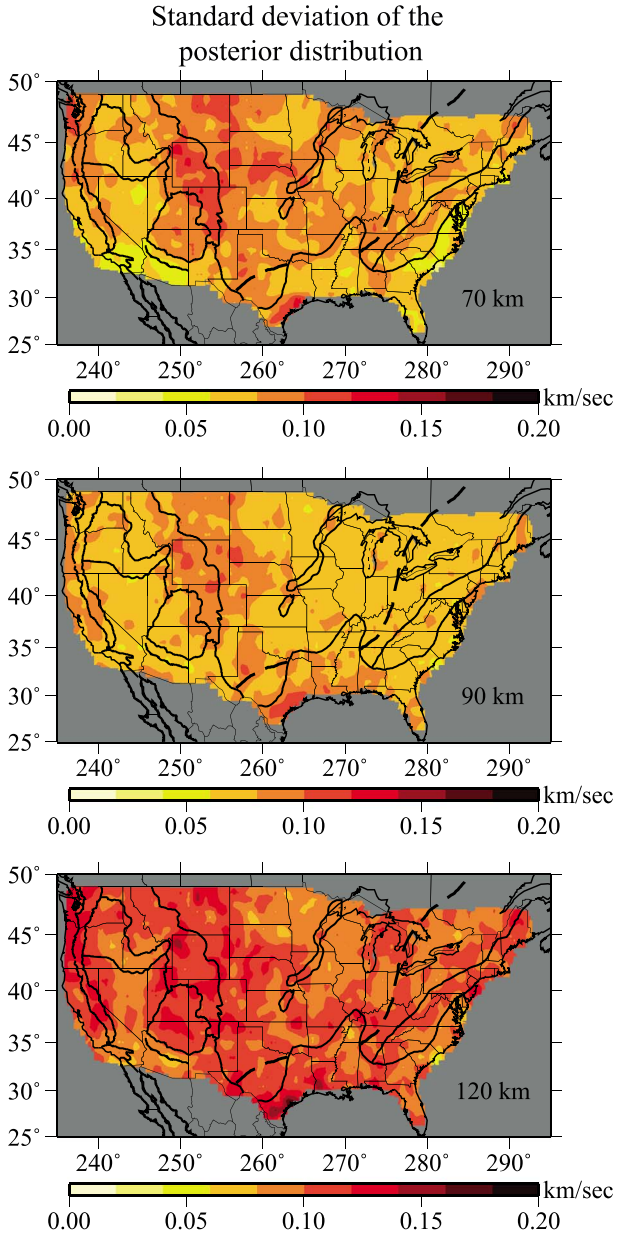

Figure 19. The standard deviation of the posterior distribution, σ_m, for V_s at different depths in the mantle within ±5 km of (d) 70 km, (e) 90 km, and (f) 120 km, respectively. This quantity is generally larger in the mantle than in the crust and grows particularly below 100 km depth.

the Reelfoot Rift, and the Appalachian Mountains with the bull's-eye of the last pair of profiles in western Virginia. The locations of these profiles are identified in Figure 20. In addition, we discuss the potential for systematic bias of the resulting 3-D model. In particular, we consider the effect of the assumed relation between V_s and density as well as our assumption of a constant intermediate Q value of 150 in the mantle.

5.1. Long East-West Transects Through the Model

Figure 21 presents vertical transects through the 3-D model across the entire U.S. along four lines of latitude: A-A′ 46.5° N, B-B′ 42°N, C-C′ 38°N, and D-D′ 34°N. As with the horizontal views of the model shown in Figures 12 and 18, the vertical transects present the mean of the posterior distribution at each depth derived from the model based on all data: surface wave dispersion, receiver functions, and Rayleigh wave H/V measurements. Each vertical transect is divided into a "crustal panel," which presents the top 60 km, and a "mantle panel," which presents depths from 30 to 150 km. The vertical exaggeration of the crustal panel is greater so that crustal features can be seen. Crustal velocities are presented as absolute quantities, but mantle velocities are presented as perturbations relative to 4.4 km/s.

Transect A-A′ goes through the northern Cascades and northern Rocky Mountain Cordillera; the Great Plains of Montana, North Dakota, and Minnesota; through the Upper Peninsula of Michigan and parts of Lake Superior, through southern Ontario and Quebec; and then terminates near the northern tip of Maine. Six model features are particularly noteworthy, which we discuss from west to east, most of which are near the western end of the profile. (1) The supraslab mantle wedge is imaged as a slow feature in the uppermost mantle beneath the Cascades. The subducting slab lies to the west of the wedge and appears as relatively fast locally. (2) Shallow low velocities underlie the Pasco basin of south-central Washington. (3) Relatively low crustal velocities lie beneath the Cordillera, although the thickest crust along the transect lies east of the Cordillera beneath the Great Plains of Montana and western North Dakota. (4) The fast mantle wave speeds of the Great Plains set on slowly east of the Cordillera through eastern Montana so that there is no abrupt onset of high mantle wave speeds in the west at this latitude. (5) In eastern North Dakota, crustal thickness reduces abruptly and enigmatically. (6) The model is relatively homogeneous from Minnesota eastward both in the crust and mantle, with the highest wave speeds in the mantle occurring from Minnesota to Michigan.

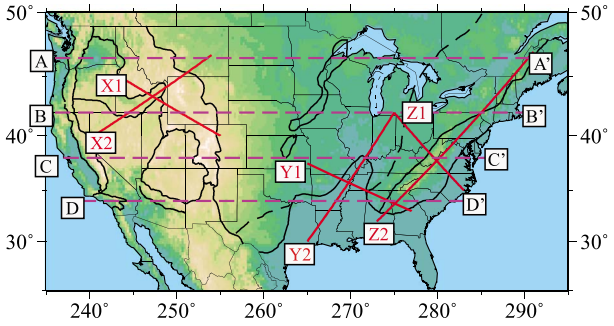

Figure 20. The location of the vertical transects through the 3-D model. Long east-west transects A-A′, B-B′, C-C′, and D-D′ are presented in Figure 21. The shorter pairs of crossing transects, X_1-X_2, Y_1-Y_2, and Z_1-Z_2, are shown in Figure 22.

Transect B-B′ extends along 42°N from the southern Cascades, through the northern Basin and Range Province and High Lava Plains, through the Wyoming Craton and central Great Plains, and terminates in eastern Massachusetts. We highlight four features from west to east. (1) The relatively high-velocity subducting slab contrasts with the exceptionally low-velocity supraslab mantle wedge, which merges with the slow upper mantle beneath the Basin and Range Province and High Lava Plains to the east. (2) The very slow Green River sediments overlie the Wyoming Craton that has velocity anomalies that amplify with depth in the mantle. (3) Relatively slow mantle velocities lie between the Wyoming Craton and the Great Plains, following the "Cheyenne Belt" [e.g., *Houston et al.*, 1989] from northeastern Colorado to the Black Hills (Figures 18b and 18c) of southwestern South Dakota. (4) Fast mantle velocities found across the eastern U.S. terminate abruptly near the edge of the northern Appalachians in eastern New York.

Transect C-C′ extends along 38°N from the Great Valley of California, through the Sierras, the Basin and Range Province, the Colorado Plateau and Rockies, and then across the central Great Plains and Appalachians to terminate near the coast of central Virginia. This transect has a large number of noteworthy features, which we again discuss them from west to east. (1) The sediments of the Great Valley appear clearly. (2) Low upper mantle velocities underlie the central Basin and Range Province beneath a clearly defined mantle lid. As seen in Figure 14, some of the strongest uppermost mantle negative vertical velocity gradients exist in the central Basin and Range Province. This is not because uppermost mantle velocities beneath the central Basin and Range Province are the lowest across the continent but because of the existence of a relative high-velocity lid right below Moho. (3) The crust and mantle of the Colorado Plateau are distinct from surrounding areas, being much faster than the Basin and Range or the Colorado Rockies. (4) In contrast, the crust and mantle of the Colorado Rockies are quite slow and the thickest crust along this transect occurs beneath the Rockies. (5) High velocities in the crust and mantle beneath the Great Plains set on rapidly east of the Rocky Mountain front, although the transition occurs near to the front in the crust and farther to the east in the mantle. (6) Low velocities occur in the mantle beneath the eastern Appalachians in western Virginia near the eastern edge of thick crust. Thinner crust is observed in eastern Virginia, but it is underlain by faster mantle.

Finally, transect D-D′ extends along 34°N from the Southern California coast near Los Angeles, through the Coastal Range and Mojave desert, through the southern Basin and Range Province, across the Rio Grande Rift, through the Southern Great Plains, the Mississippi Embayment and the Reelfoot Rift, and the southern Appalachians to terminate near the coast of southern North Carolina. (1) Low-velocity mantle underlies the Mohave desert and southern Basin and Range Province, but as with the Basin and Range farther north there is a significant relative high-velocity lid in the uppermost mantle. (2) The lowest mantle wave speeds lie beneath the Rio Grande Rift, and they are shallower than the lowest velocities beneath the Basin and Range Province. (3) The Great Plains high velocities in the mantle set on abruptly near the eastern terminus of the Rio Grande Rift. (4) At this latitude, the thickest Mississippi Embayment sediments lie just to the west of the Reelfoot Rift, which appears as a shallow mantle relative low-velocity feature. (5) Relatively low wave speeds in the uppermost mantle extend from the Reelfoot Rift in southern Arkansas across the southern U.S. to eastern South Carolina and then are replaced by faster mantle shear wave speeds nearer to the Atlantic coast.

5.2. Shorter Crossing Transects Through the Model

The transects X_1 and X_2 in Figure 22a run along and across the Snake River Plain (SNP). Profile X_2 runs along the SNP. The slow mantle velocities predominantly lie between depths of 50 and 100 km, deepen slightly to the southwest along the SNP, and are slowest where the SNP crosses 42.7°N latitude, which is considerably west of Yellowstone. The crossing profile, X_1, illustrates the cross-sectional width of the low-velocity anomaly in the mantle beneath the SNP. This profile also contrasts the SNP low-velocity anomaly with the high

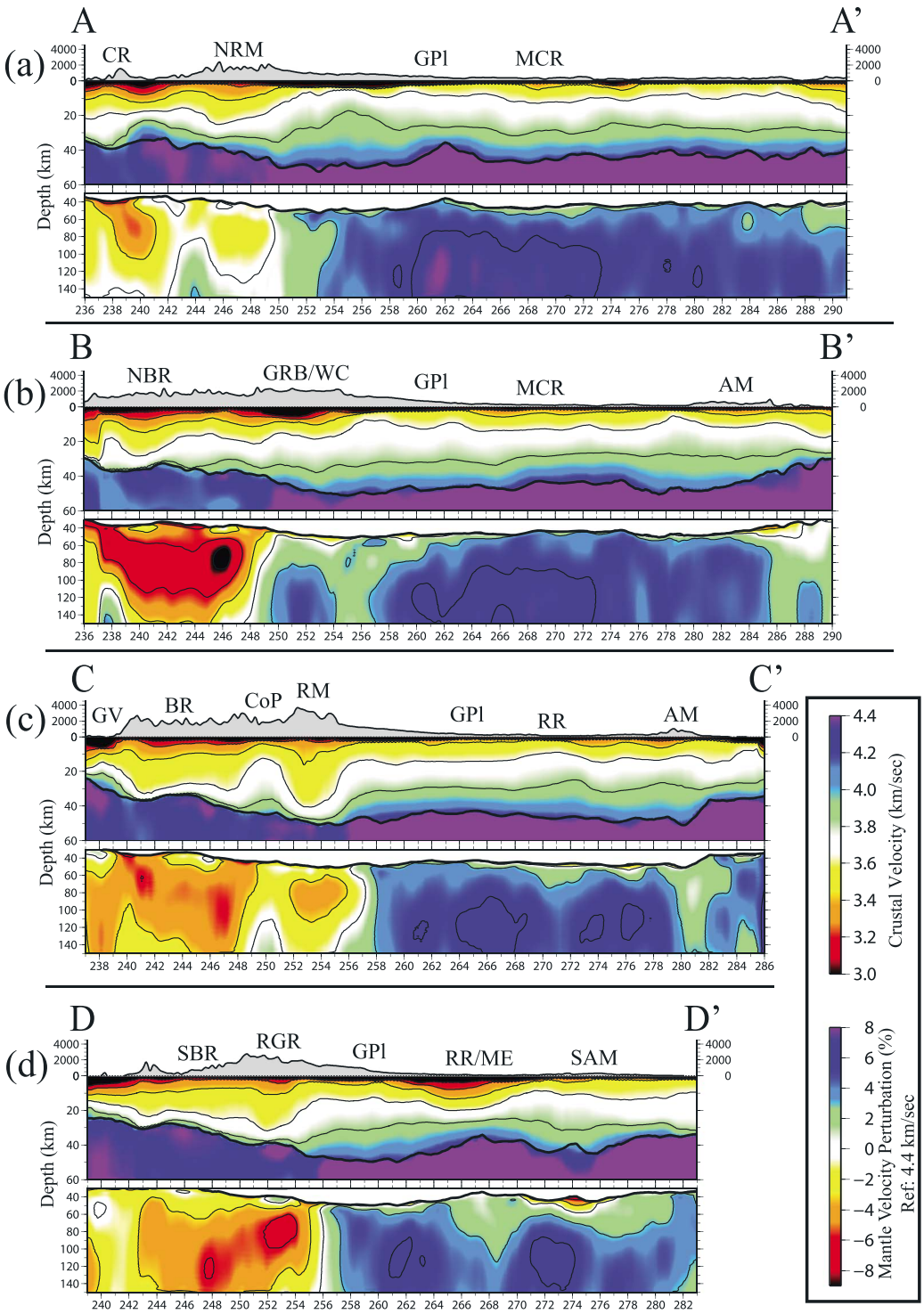

Figure 21. Four east-west oriented vertical transects through the 3-D model, with locations identified in Figure 20, defined as the mean of the posterior distribution of V_s at each location and depth. Each transect is part of a pair of depth profiles with different vertical exaggerations: one for the crust (top 60 km) and the other for the uppermost mantle (30–150 km). Depth is defined as the distance below the free surface, absolute crustal velocities are presented according to the inset legend, crustal thickness is identified with a bold solid black line, isolines in the crust and mantle are placed at intervals of 0.2 km/s and 3%, respectively, and mantle velocities are presented as perturbations relative to 4.4 km/s in percent. Local surface topography is also indicated, as are abbreviated names of selected structural and geographic features, most of which are identified in Table 1 with the exception of NRM (northern Rocky Mountains), NBR, and SBR (northern and southern Basin and Range, respectively).

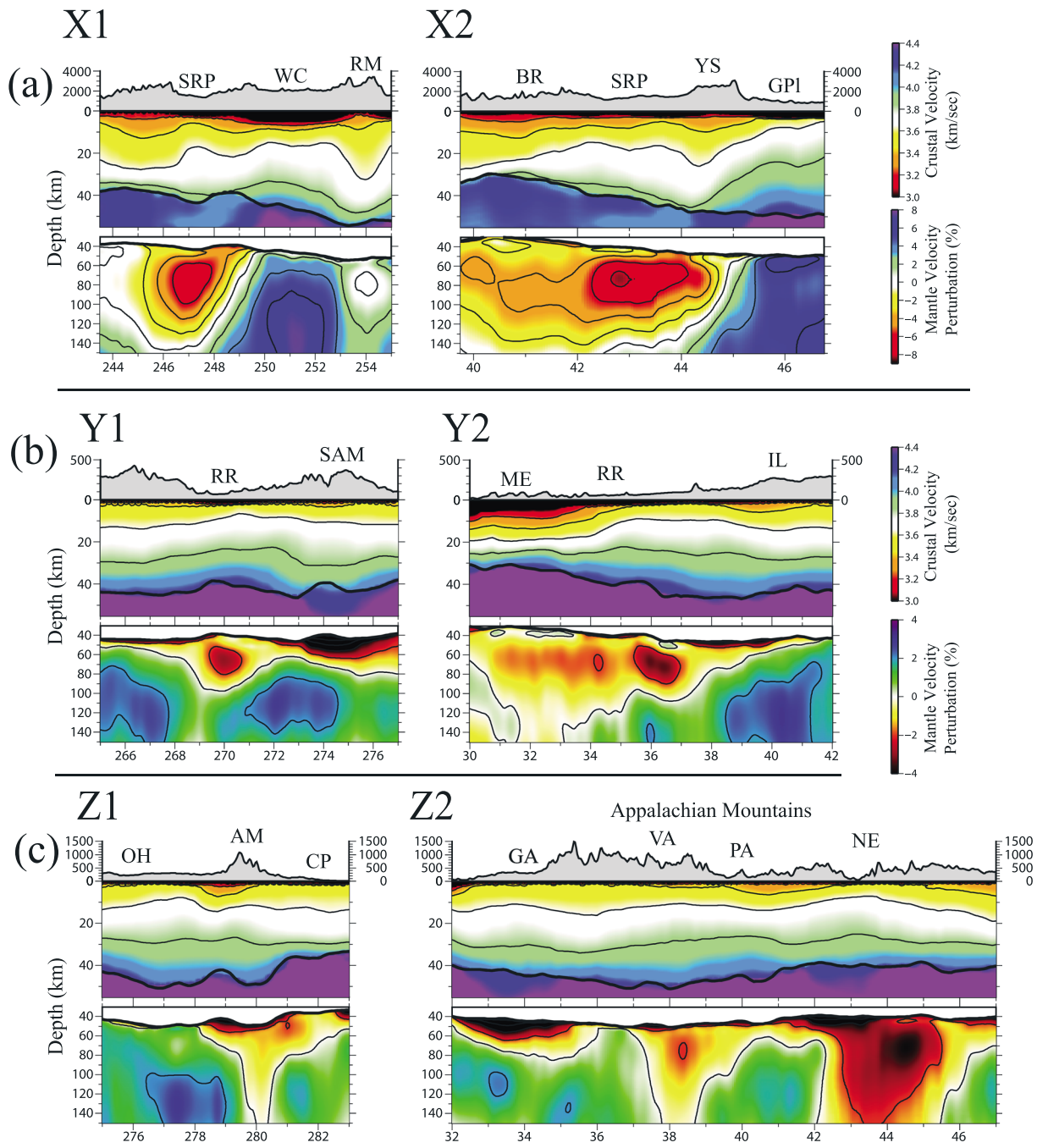

Figure 22. Three pairs of shorter crossing vertical transects with locations identified in Figure 20. Profiles X_1 and X_2 are oriented along and across the Snake River Plain, profiles Y_1 and Y_2 target the Reelfoot Rift, and profiles Z_1 and Z_2 target the Appalachians, crossing in western Virginia. Definitions and formatting are similar to Figure 21 but there are differences. Crustal velocities are presented on the same absolute scale as in Figure 21 and mantle velocities are perturbations relative to a constant value, but the mantle reference for profiles X_1 and X_2 is 4.3 km/s and the reference for profiles Y_1, Y_2, Z_1, and Z_2 is 4.55 km/s. The color scale for profiles X_1 and X_2 ranges between ±8%, as in Figure 21, but the scale for the other profiles ranges only between ±4%. Abbreviations are identified in Table 1 with the exception of SAM (southern Appalachian Mountains).

velocities beneath the Wyoming Craton southeast of the SNP. The velocity anomaly beneath the Wyoming Craton intensifies with depth in contrast to the shallower focus of the low-velocity anomaly beneath the SNP.

Transects Y_1 and Y_2 in Figure 22b run through a geologically much older feature, the Reelfoot Rift. The amplitude of the velocity anomaly is, therefore, smaller. The profile along the rift, Y_2, shows that the lowest mantle shear wave speeds lie between depths of about 50 and 90 km. The lowest velocities lie in a nearly horizontal

band, but relatively low-velocity anomalies extend deeper into the mantle in the southwestern part of the profile. The crust thickens along the rift to the northeast and becomes faster in the northern part of the rift compared to the southern rift, as evidenced by upward curved crustal isolines. The crossing profile, Y_1, reveals the width of the mantle low-velocity anomaly. The low-velocity anomaly beneath the far southern extent of the Appalachians in the shallow mantle also can be seen in profile Y_1.

Transects Z_1 and Z_2 in Figure 22c lie along and transverse to the Appalachian Mountains, crossing in western Virginia. Transect Z_2 highlights that along the Appalachians there are three centers with mantle low-velocity anomalies: beneath northern Georgia, beneath the Blue Ridge Mountains of western Virginia, and below the Green Mountains and White Mountains of New England. The transverse profile in Z_1 goes through western Virginia and shows that the anomaly is concentrated in the shallow mantle but extends through the model to at least 150 km. This is in contrast to the northern Georgia anomaly, which is confined to the shallow mantle above 80 km depth, but is similar to the anomaly beneath New England. The New England velocity anomaly is considerably stronger than the other two along the Appalachians and is arguably stronger than the anomaly that underlies the Reelfoot Rift. We note that *Chu et al.* [2013] discuss a potential Cretaceous hot spot track that would lie along the central and northern Appalachians, from western Virginia into New England where mantle low velocities are seen in Figure 22c.

Due to different average velocities in the mantle and different color scales it may not be immediately obvious that the velocity anomalies in Figure 22 beneath the Snake River Plain are much slower than beneath the Reelfoot Rift and the Appalachians. The lowest velocities beneath the Snake River Plain are about 8% below 4.3 km/s (~3.96 km/s), but the lowest velocities beneath New England are only about 4% below 4.55 km/s (~4.36 km/s). Nevertheless, mantle structure beneath the Reelfoot Rift and the Appalachians illustrates that significant mantle heterogeneity occurs across the eastern and Central U.S.

5.3. Potential for Systematic Error

In section 4.2, we considered the estimate of model error, $<e_{\overline{m}}>$, to be composed of systematic and nonsystematic or random components:

$$< e_{\overline{m}} >=< e_{\mathrm{sys}} > + < e_{\mathrm{nonsys}} > . \tag{10}$$

We argued that $<e_{\mathrm{nonsys}}>$ should encompass model fluctuations and will be controlled predominantly by errors in the data and trade-offs between model variables at different depths. We came to identify it with the standard deviation of the mean of the posterior distribution at each location and depth:

$$< e_{\mathrm{nonsys}} >= \sigma_{\overline{m}}. \tag{11}$$

We computed $\sigma_{\overline{m}}$ by scaling the standard deviation of the posterior distribution, $\sigma_{\overline{m}}$, inversely by the square root of the number of independent models in the posterior distribution and estimated this number by considering the characteristics of the likelihood function as suggested by *Mosegaard and Tarantola* [1995]. We found on average that to compute $\sigma_{\overline{m}}$, we needed to scale σ_m by 1/4–1/5. On average, this result captures our degree of belief in the models concerning the effect of random or nonsystematic errors in the mean of the posterior. Estimates of random error are designed to capture model stability and quantify the degree of fluctuation in the model that results from measurement error. However, as we discuss here, systematic errors may be considerably larger than random errors and random error estimates should be seen as providing a lower bound on the likely errors in the resulting model.

The evaluation of systematic errors in the resulting model is a thornier subject than random errors because it involves an assessment of the effect of assumptions and constraints imposed in the inversion in the final models, and we do not know how the Earth deviates from our assumptions. Three of the most important effects to consider are (1) the scaling of V_p with V_s, (2) the scaling of density (ρ) with V_s, and (3) the choice of Q in the mantle. The effect of the choice of Q on the estimated model arises through the correction for physical dispersion [*Kanamori and Anderson*, 1977], which is strongest when Q is low. The large Q of the crust mitigates the effect on our model of ignorance of its exact value, but Q in the mantle is typically much smaller, which means that ignorance of mantle Q may have a more significant impact on the estimated model. The assumptions we made about V_p, ρ, and Q are discussed in section 3.1, in equations (1) and (2), and the paragraph that follows them.

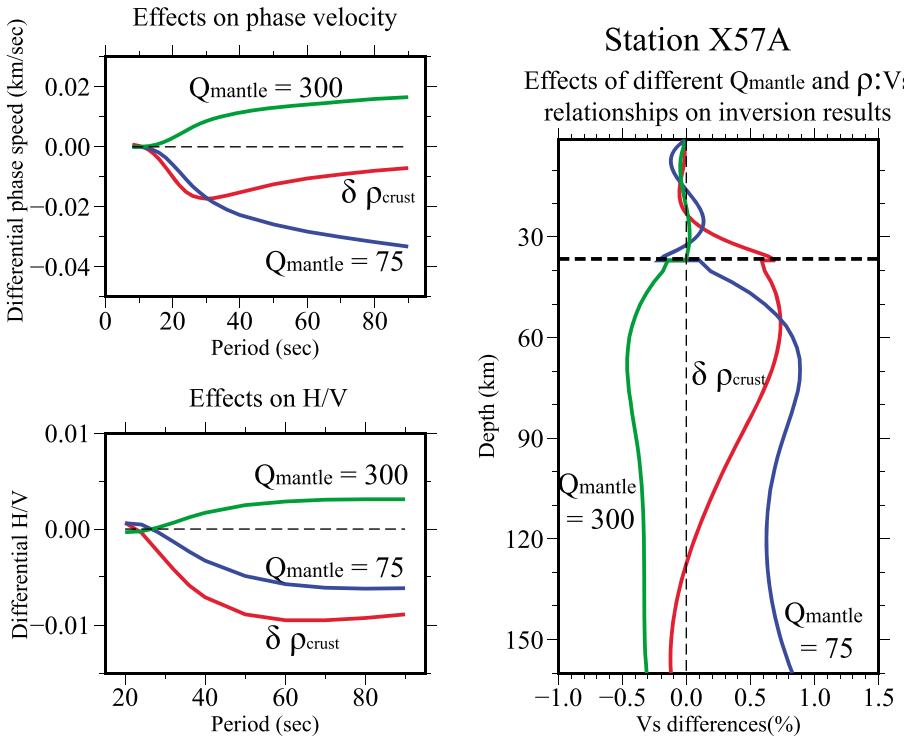

Figure 23. Simulated effects of systematic errors evaluated by (blue lines) changing *Q* from 150 to 75 in the mantle, (green lines) changing *Q* from 150 to 300 in the mantle, and (red lines) increasing density by 0.1 g/cm^3 throughout the crystalline crust. (a) Effect on Rayleigh wave phase velocity as a function of period. (b) Same as in Figure 23a but for the effect on Rayleigh wave ellipticity, *H/V*. (c) The effect on the estimated mean of the posterior distribution of V_s. All results are presented by perturbing around the mean of the posterior distribution for station X57A (Hartsville, SC).

Shen et al. [2013b] discussed at some length the effect of varying the V_p/V_s ratio in the inversion. They introduced the crustal V_p/V_s ratio as a variable in their inversion and found two important effects. First, they found that using surface wave dispersion data and receiver functions truncated 10 s after the *P* phase arrival, the posterior distribution of V_p/V_s was approximately uniform. This means that V_p/V_s could not be estimated with the data they used. We introduce Rayleigh wave *H/V* measurements relative to their data set but do not believe that this will influence the posterior distribution of V_p/V_s appreciably. Second, they found that the choice of the V_p/V_s ratio dominantly affected their estimate of crustal thickness. Varying V_p/V_s from 1.70 to 1.80, for example, changes the mean of the posterior distribution for crustal thickness by about 3 km, on average. Thus, a reasonable estimate of the effect on crustal thickness of variations in V_p/V_s around the value of 1.75 that we impose in the crust is about ±1.5 km. This will impact regions where receiver functions constrain crustal thickness in our model and, therefore, will exclude sedimentary basins where reverberations in the receiver functions typically obscure the observation of the time of the Moho phase conversion. The standard deviation of the mean of crustal thickness in the posterior distribution (divided by 4–5; Figure 13b) is on average about 1 km across the U.S. Thus, the systematic error caused by V_p/V_s deviating from our assumed value of 1.75 in the crust may very well be larger than random error in some locations.

We now discuss systematic effects on the estimated models due to *Q* in the mantle differing from our assumption of 150 and ρ in the crust differing from the relation with V_s given by equation (2). The results we present here are shown for the inversion at station X57A in Hartsville, SC. Results at other stations are similar but not identical.

Rayleigh wave phase speeds are sensitive to *Q* because V_s presented in the model depends on the physical dispersion correction [*Kanamori and Anderson*, 1977]. Figure 23a illustrates the effects on Rayleigh wave phase speed of changing *Q* in the mantle from 150 to both 75 and 300 using blue and green lines, respectively. The effect on *H/V* measurements is shown in Figure 23b. Halving *Q* from 150 to 75 has a larger effect than doubling *Q* from 150 to 300 on Rayleigh wave phase speeds and *H/V* measurements. The effect on

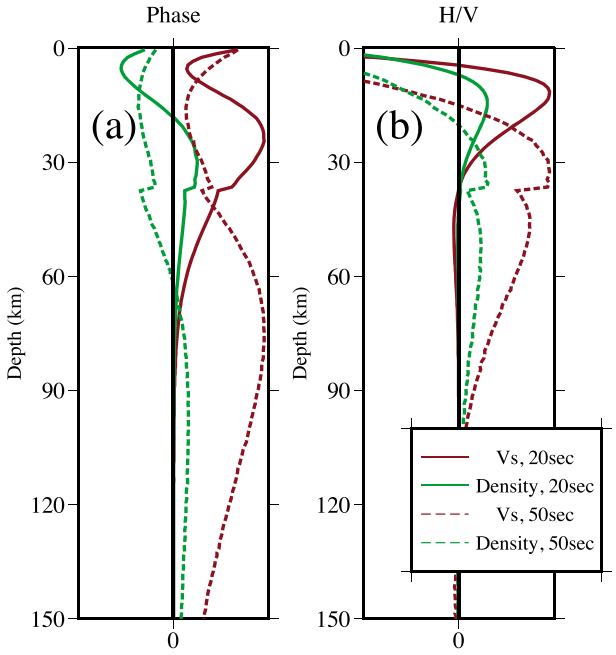

Figure 24. Sensitivity of (a) Rayleigh wave phase speed and (b) ellipticity (*H*/*V*) to perturbations in (red lines) V_s and (green lines) density at periods of 20 s and 50 s.

estimates of the mean of the posterior distribution of changing mantle *Q* from 150 to 75 and 300 is shown in Figure 23c. The effect is largely confined to the mantle with much smaller effects in the crust. If mantle *Q* were in fact 75 rather than the 150 we assumed, then the estimated V_s in the mantle would be increased by about 0.7% on average from 60 to 150 km depth. In contrast, if *Q* were actually 300, then the estimated V_s in the mantle would be decreased on average by about 0.4% in the same depth range. Because much of the western U.S. probably may have a lower mantle *Q* than 150 and the eastern U.S. probably has a larger *Q* than this value [*Dalton et al.*, 2008], model bias due to the assumed *Q* model is probably larger in the west than in the east. The net impact is that our estimate of mantle V_s in the west may be biased low by in excess of 0.5%. The V_s values we estimated in the east may be biased high by this effect by a smaller value, perhaps in excess of 0.25%. The bias in the east due to uncertainty in *Q* probably lies within the standard deviation of the mean, which we equate with random error, but the bias in the west may be larger than our estimate of random error. However, both in the west and in the east, the bias may be spatially coherent over large areas.

Rayleigh wave phase speeds and *H*/*V* measurements also possess sensitivity to crustal density. Figure 24 presents sensitivity kernels showing the sensitivity of Rayleigh wave phase speeds and *H*/*V* measurements to density and V_s perturbations. An important difference is that for phase speeds the density kernel changes sign. A positive V_s perturbation in the crust will produce a positive perturbation in Rayleigh wave phase speed, but a positive crustal density perturbation will produce an effect on phase speed that could be positive, negative, or zero depending on period and how the perturbation is distributed vertically in the crust. However, for density perturbations that are focused on the top half of the crust, a positive crustal density perturbation will produce a negative effect on phase speed. For *H*/*V*, the shapes of the V_s and density kernels are similar and both change sign with depth. However, the largest kernel amplitudes are negative and near the surface. Again, if perturbations are focused in the upper half of the crust, then positive perturbations in density or V_s will produce negative perturbation on *H*/*V*. Finally, it is worth noting that for kernels that change sign in the crust, the effect of perturbations applied across the whole crust will tend to cancel. As described in the next paragraph, we apply a constant crustal density perturbation across the entire crust. Thus, the effect both on phase speeds and *H*/*V* is mostly at long periods where the sign change of the kernel occurs in the mantle.

Figures 23a and 23b show the impact on phase speed and *H*/*V* measurements of changing crustal density by 0.1 g/cm^3 across the entire crust relative to the value given by equation (2). This perturbation ranges from 3% to 4% depending on depth in the crust. A positive crustal density perturbation will decrease phase speed at all periods, but due to the oscillation of the sensitivity kernel in the crust at short periods, the impact will be experienced dominantly at intermediate periods (Figure 23a). Similarly, the impact on *H*/*V* will predominantly be at longer periods (Figure 23b). Bias of the model, therefore, will mostly be confined to the uppermost mantle as Figure 23c illustrates. A systematic error of density of 3%–4% across the entire crust would produce a bias in V_s of 0.6%–0.8% from the Moho to about 100 km depth in the mantle, with a smaller effect in the lowermost crust. The details of the bias will depend on the vertical distribution of the density error, but we believe that systematic errors in the mantle of 0.5% may be common. If density errors are not distributed as evenly in the crust, then a bias of crustal V_s could occur.

In summary, we have discussed three potential sources of systematic error here: the scaling relation between V_p and V_s, the scaling relation between density and Vs, and the assumed value of Q in the mantle. We believe that errors in the assumed crustal V_p/V_s ratio mostly likely will bias estimates of crustal thickness. Errors of up to 1.5 km are to be expected in some places, which is larger than average random error across the U.S. (~1 km). The impact of error in the assumed crustal density on estimated model V_s will depend in detail on the vertical distribution of the error in density, but we show that (perhaps contrary to expectation) model bias in the mantle can be appreciable. We show that a systematic error in crustal density across the entire crust of 3%–4% can bias V_s in the uppermost mantle by more than 0.5%, which is larger than average random error. Finally, errors in Q assumed in the mantle will also bias estimated V_s in the mantle. We discuss ways in which systematic errors may be reduced in the future in section 6.

6. Conclusions

We present a 3-D model of crustal and uppermost mantle V_s to a depth of about 150 km across the contiguous U.S. The model is constructed from a set of vertical 1-D profiles beneath 1816 USArray Transportable Array (TA) stations produced by jointly inverting Rayleigh wave dispersion, receiver functions, and Rayleigh wave ellipticity (H/V) measurements. Rayleigh wave dispersion curves are derived from ambient noise and earthquakes, which agree in the period band of overlap. Estimates of measurement error for all data allow us to invert the different data sets together. A Bayesian Monte Carlo procedure provides the basis for the inversion and a posterior distribution of models is constructed beneath each TA station. We summarize these distributions at each location and depth with the mean, $\overline{m}$, and standard deviation, σ_m, and we then interpolate these depth-dependent statistics onto a 0.25°×0.25° across the U.S. by simple kriging. The resulting depth-dependent interpolated pair ($\overline{m}$ and σ_m) as a function of depth across the U.S. forms the 3-D model.

We argue here that the standard deviation of the posterior distribution, σ_m, is not an ideal estimate of absolute model uncertainty, but it provides useful information about relative uncertainty. It is too large to represent random error and does not include an estimate of systematic error. A better estimate of random or nonsystematic error of the model is the standard deviation of the mean of the posterior distribution, $\sigma_{\overline{m}}$. This statistic provides a better estimate of the fluctuations observed in the 3-D model and more accurately reflects the impact on model variables of data uncertainties. Using two different methods, we demonstrate that on average $\sigma_{\overline{m}}$ can be estimated by scaling σ_m by about 0.2–0.25. Doing so, we find that nonsystematic model error in V_s averages about 0.2% in the midcrust and 0.4% in the mantle, but these errors grow near Moho and the free surface.

A great many structural features are determined reliably in the 3-D model. We do not focus here on interpreting these features or even pointing them out systematically but provide views of the model across the continent. We do highlight three prominent features of the model beneath and across the Snake River Plain, the Reelfoot Rift, and the Appalachian Mountains. The observation of three low-velocity features beneath the Appalachians in western Virginia, northern Georgia, and New England is new to the best of our knowledge. We believe that the explication of the model will require a number of papers dedicated to individual structural features, such as the paper on the Mid-Continent Rift by *Shen et al.* [2013c].

Although we discuss random or nonsystematic error at some length, systematic error is probably larger and of greater concern because it is more difficult to estimate reliably. Systematic error results from the deviation of the constraints and assumptions that we impose in the inversion from the real Earth. Our discussion of systematic error aims to quantify the probable magnitude and nature of several important types of error. In so doing, it provides the basis to identify fruitful directions to advance the model as part of future research.

We discuss three potential sources of systematic error here: deviation of crustal V_p/V_s from 1.75, the introduction of a crustal density perturbation relative to the assumed ρ:V_s scaling relation given by equation (2), and deviation of mantle Q from the value of 150 assumed in our inversion. We find that systematic errors are most likely to accrue to estimates of crustal thickness and V_s in the mantle. Even crustal density errors, if they persevere throughout the crust, will manifest dominantly as bias of V_s in the mantle rather than in the crust, although bias of crustal V_s is also possible if density error is confined to shallow depths. Such systematic errors arising from several separate sources may constructively or destructively interfere with one another, but errors of 0.5%–1% in V_s at upper mantle depths are probably not unlikely, which is larger than average

random error. Such errors may be coherent over large regions (e.g., mantle Q in the west may be consistently lower than 150 and in the east consistently higher) or may vary rapidly laterally (e.g., geological variations affecting crustal density).

Future research is called for that will beat down systematic error by introducing better information in the inversion to improve constraints on V_P, density, and mantle Q. For example, V_P/V_S can be better constrained by introducing longer P-to-S receiver functions into the analysis [e.g., *Zhu and Kanamori*, 2000; *Chen and Niu*, 2013]. S-to-P receiver functions would also provide new and valuable constraints [e.g., *Hansen and Dueker*, 2009; *Lekić and Fischer*, 2014; *Fischer*, 2015]. In addition, a more accurate density-to-V_S scaling relationship may arise by applying gravity [e.g., *Maceira and Ammon*, 2009] and surface wave local amplification data in the inversion simultaneously [e.g., *Eddy and Ekström*, 2014; *Lin et al*., 2012a]. Moreover, there are many other fruitful directions to improve and extend the model presented here in future work. We mention only three. First, it will be important to include the introduction of Love waves, which will provide information about radial anisotropy [e.g., *Moschetti et al*., 2010a, 2010b; *Xie et al*., 2013]. Second, it is also important to perform the simultaneous interpretation of Rayleigh wave azimuthal anisotropy [e.g., *Lin et al*., 2011] with other data in order to constrain the full elasticity tensor [e.g., *Xie et al*., 2015]. Third, the increasing availability of dense (large N) arrays improves the ability to constrain discontinuities in the interior of the crust, which are not included in the present study [e.g., *Deng et al*., 2015].

Acknowledgments

The authors thank the Associate Editor, Antonio Villasenor, and an anonymous reviewer for their comments that have helped to improve this paper. They also thank Fan-Chi Lin and Vera Schulte-Pelkum for their valuable conversations and Lili Feng for the help in preparing some of the ambient noise measurements. The facilities of the IRIS Data Management System, and specifically the IRIS Data Management Center, were used to access the waveform and metadata required in this study. The IRIS DMS is funded through the National Science Foundation and specifically the GEO Directorate through the Instrumentation and Facilities Program of the National Science Foundation under Cooperative Agreement EAR-0552316. This work was supported by NSF grant EAR-1252085 at the University of Colorado at Boulder. This work utilized the Janus supercomputer, which is supported by the National Science Foundation (award CNS-0821794), the University of Colorado at Boulder, the University of Colorado Denver, and the National Center for Atmospheric Research. The Janus supercomputer is operated by the University of Colorado at Boulder. The 3-D model (i.e., the mean of the posterior distribution) together with its attendant uncertainties (i.e., the standard deviation of the posterior distribution) are available via the IRIS Earth Model Collaboration [*Trabant et al.*, 2012] at http://ds.iris.edu/ds/products/emc/. At the time of publication, the model, uncertainties, and the dispersion maps are also available via the CU-Boulder Web site at http://ciei.colorado.edu/Models and http://ciei.colorado.edu/DispMaps.

References

Agrawal, M., J. Pulliam, M. K. Sen, and H. Gurrola (2015), Lithospheric structure of the Texas-Gulf of Mexico passive margin from surface wave dispersion and migrated P_s receiver functions, *Geochem. Geophys. Geosyst.*, *16*, 2221–2239, doi:10.1002/2015GC005803.

Allison, C. M., R. C. Porter, M. J. Fouch, and S. Semken (2013), Seismic evidence for lithospheric modification beneath the Mojave Neovolcanic Province, Southern California, *Geophys. Res. Lett.*, *40*, 5119–5124, doi:10.1002/grl.50993.

Bailey, I. W., M. S. Miller, K. Liu, and A. Levander (2012), V_S and density structure beneath the Colorado Plateau constrained by gravity anomalies and joint inversions of receiver function and phase velocity data, *J. Geophys. Res.*, *117*, B02313, doi:10.1029/2011JB008522.

Barmin, M. P., M. H. Ritzwoller, and A. L. Levshin (2001), A fast and reliable method for surface wave tomography, *Pure Appl. Geophys.*, *158*(8), 1351–1375.

Benoit, M. H., C. Ebinger, and M. Crampton (2014), Orogenic bending around a rigid Proterozoic magmatic rift beneath the central Appalachian Mountains, *Earth Planet. Sci. Lett.*, *402*, 197–208.

Bensen, G. D., M. H. Ritzwoller, M. P. Barmin, A. L. Levshin, F. Lin, M. P. Moschetti, N. M. Shapiro, and Y. Yang (2007), Processing seismic ambient noise data to obtain reliable broad-band surface wave dispersion measurements, *Geophys. J. Int.*, *169*, 1239–1260, doi:10.1111/j.1365-246X.2007.03374.x.

Bensen, G. D., M. H. Ritzwoller, and Y. Yang (2009), A 3D shear velocity model of the crust and uppermost mantle beneath the United States from ambient seismic noise, *Geophys. J. Int.*, *177*(3), 1177–1196.

Bodin, T., M. Sambridge, H. Tkalčić, P. Arroucau, K. Gallagher, and N. Rawlinson (2012), Transdimensional inversion of receiver functions and surface wave dispersion, *J. Geophys. Res.*, *117*, B02301, doi:10.1029/2011JB008560.

Boore, D. M., and M. N. Toksoz (1969), Rayleigh wave particle motion and crustal structure, *Bull. Seismol. Soc. Am.*, *59*(1), 331–346.

Boué, P., P. Roux, M. Campillo, and X. Briand (2014), Phase velocity tomography of surface waves using ambient noise cross correlation and array processing, *J. Geophys. Res. Solid Earth*, *119*, 519–529, doi:10.1002/2013JB010446.

Brocher, T. M. (2005), Empirical relations between elastic wave speeds and density in the Earth's crust, *Bull. Seismol. Soc. Am.*, *95*, 2081–2092, doi:10.1785/0120050077.

Calkins, J. A., G. Zandt, J. Girardi, K. Dueker, G. E. Gehrels, and M. N. Ducea (2010), Characterization of the crust of the Coast Mountains Batholith, British Columbia, from P to S converted seismic waves and petrologic modeling, *Earth Planet. Sci. Lett.*, *289*(1), 145–155.

Calkins, J. A., G. A. Abers, G. Ekstrom, K. C. Creager, and S. Rondenay (2011), Shallow structure of the Cascadia subduction zone beneath western Washington from spectral ambient noise correlation, *J. Geophys. Res.*, *116*, B07302, doi:10.1029/2010JB007657.

Chang, S. J., C. E. Baag, and C. A. Langston (2004), Joint analysis of teleseismic receiver functions and surface wave dispersion using the genetic algorithm, *Bull. Seismol. Soc. Am.*, *94*(2), 691–704.

Chen, Y., and F. Niu (2013), Ray-parameter based stacking and enhanced pre-conditioning for stable inversion of receiver function data, *Geophys. J. Int.*, *204*(3), doi:10.1093/gji/ggt179.

Chu, R., and D. Helmberger (2014), Lithospheric waveguide beneath the Midwestern United States; massive low-velocity zone in the lower crust, *Geochemistry, Geophysics, Geosystems*, *15*, 1348–1362, doi:10.1002/2013GC004914.

Chu, R., W. Leng, D. V. Helmberger, and M. Gurnis (2013), Hidden hotspot track beneath the eastern United States, *Nat. Geosci.*, doi:10.1038/NGEO1949.

Dalton, C. A., G. Ekström, and A. M. Dziewoński (2008), The global attenuation structure of the upper mantle, *J. Geophys. Res.*, *113*, B09303, doi:10.1029/2007JB005429.

Delorey, A. A., and J. E. Vidale (2011), Basin shear-wave velocities beneath Seattle, Washington, from noise-correlation Rayleigh waves, *Bull. Seismol. Soc. Am.*, *101*(5), 2162–2175.

Deng, Y., W. Shen, T. Xu, and M. H. Ritzwoller (2015), Crustal layering in northeastern Tibet: A case study based on joint inversion of receiver functions and surface wave dispersion, *Geophys. J. Int.*, *203*(1), 692–706.

Dziewonski, A. M., and D. L. Anderson (1981), Preliminary reference Earth model, *Phys. Earth Planet. Inter.*, *25*(4), 297–356.

Eagar, K. C., M. J. Fouch, D. E. James, and R. W. Carlson (2011), Crustal structure beneath the High Lava Plains of eastern Oregon and surrounding regions from receiver function analysis, *J. Geophys. Res.*, *116*, B02313, doi:10.1029/2010JB007795.

Eddy, C. L., and G. Ekström (2014), Local amplification of Rayleigh waves in the continental United States observed on the USArray, *Earth Planet. Sci. Lett.*, *402*, 50–57.

Ekström, G. (2014), Love and Rayleigh phase-velocity maps, 5–40 s, of the western and Central USA from USArray data, *Earth Planet. Sci. Lett.*, *402*, 42–49.
Fenneman, N. M., and D. W. Johnson (1946), *Physical Divisions of the United States*, U.S. Geol. Surv., Washington, D. C.
Fischer, K. M. (2015), Crust and lithospheric structure—Seismological constraints on the lithosphere-asthenosphere boundary, *Treatise Geophys.*, 587–612.
Frassetto, A. M., G. Zandt, H. Gilbert, T. J. Owens, and C. H. Jones (2011), Structure of the Sierra Nevada from receiver functions and implications for lithospheric foundering, *Geosphere*, *7*(4), 898–921.
Fu, Y. V., and A. Li (2015), Crustal shear wave velocity and radial anisotropy beneath the Rio Grande rift from ambient noise tomography, *J. Geophys. Res. Solid Earth*, *120*, 1005–1019, doi:10.1002/2014JB011602.
Gaite, B., A. Iglesias, A. Villaseñor, M. Herraiz, and J. F. Pacheco (2012), Crustal structure of Mexico and surrounding regions from seismic ambient noise tomography, *Geophys. J. Int.*, *188*(3), 1413–1424.
Gao, H. (2015), Crustal seismic structure beneath the source area of the Columbia River flood basalt: Bifurcation of the Moho driven by lithosphere delamination, *Geophys. Res. Lett.*, *42*, 9764–9771, doi:10.1002/2015GL066625.
Gao, H., and Y. Shen (2012), Validation of shear-wave velocity models of the Pacific Northwest, *Bull. Seismol. Soc. Am.*, *102*(6), 2611–2621.
Gao, H., E. D. Humphreys, H. Yao, and R. D. van der Hilst (2011), Crust and lithosphere structure of the northwestern US with ambient noise tomography: Terrane accretion and Cascade arc development, *Earth Planet. Sci. Lett.*, *304*(1), 202–211.
Gashawbeza, E. M., S. L. Klemperer, C. K. Wilson, and E. L. Miller (2008), Nature of the crust beneath northwest Basin and Range Province from teleseismic receiver function data, *J. Geophys. Res.*, *113*, B10308, doi:10.1029/2007JB005306.
Gilbert, H. (2012), Crustal structure and signatures of recent tectonism as influenced by ancient terranes in the western United States, *Geosphere*, *8*(1), 141–157.
Hacker, B. R., and G. A. Abers (2004), Subduction Factory 3: An Excel worksheet and macro for calculating the densities, seismic wave speeds, and H_2O contents of minerals and rocks at pressure and temperature, *Geochem. Geophys. Geosyst.*, *5*, Q01005, doi:10.1029/2003GC000614.
Hansen, S., and K. Dueker (2009), *P*- and *S*-wave receiver function images of crustal imbrication beneath the Cheyenne Belt in southeast Wyoming, *Bull. Seismol. Soc. Am.*, *99*(3), 1953–1961.
Hansen, S. M., K. G. Dueker, J. C. Stachnik, R. C. Aster, and K. E. Karlstrom (2013), A rootless rockies—Support and lithospheric structure of the Colorado Rocky Mountains inferred from CREST and TA seismic data, *Geochem. Geophys. Geosyst.*, *14*, 2670–2695, doi:10.1002/ggge.20143.
Hopper, E., H. A. Ford, K. M. Fischer, V. Lekic, and M. J. Fouch (2014), The lithosphere–asthenosphere boundary and the tectonic and magmatic history of the north-western United States, *Earth Planet. Sci. Lett.*, *402*, 69–81.
Houston, R. S., E. M. Duebendorfer, K. E. Karlstrom, and W. R. Premo (1989), A review of the geology and structure of the Cheyenne belt and Proterozoic rocks of southern Wyoming, *Geol. Soc. Am. Spec. Pap.*, *235*, 1–12.
Jin, G., and J. B. Gaherty (2015), Surface wave phase-velocity tomography based on multichannel cross-correlation, *Geophys. J. Int.*, *201*(3), 1383–1398.
Jones, C. H., and R. A. Phinney (1998), Seismic structure of the lithosphere from teleseismic converted arrivals observed at small arrays in the southern Sierra Nevada and vicinity, California, *J. Geophys. Res.*, *103*(B5), 10,065–10,090, doi:10.1029/97JB03540.
Julia, J., C. J. Ammon, R. B. Herrmann, and A. M. Correig (2000), Joint inversion of receiver function and surface wave dispersion observations, *Geophys. J. Int.*, *143*(1), 99–112.
Kanamori, H., and D. Anderson (1977), Importance of physical dispersion in surface wave and free oscillation problems: Review, *Revs. Geophys. Space Phys.*, *15*(1), 105–112, doi:10.1029/RG015i001p00105.
Kang, D., W. Shen, J. Ning, and M. H. Ritzwoller (2016), Seismic evidence for lithospheric modification associated with intra-continental volcanism in northeastern China, *Geophys. J. Int.*, *204*(1), 215–235.
Kao, H., Y. Behr, C. Currie, R. Hyndman, J. Townend, F.-C. Lin, M. H. Ritzwoller, S.-J. Shan, and J. He (2013), Ambient seismic noise tomography of Canada and adjacent regions: Part I. Crustal structures, *J. Geophys. Res. Solid Earth*, *118*, 5865–5887, doi:10.1002/2013JB010535.
Last, R. J., A. A. Nyblade, C. A. Langston, and T. J. Owens (1997), Crustal structure of the East African Plateau from receiver functions and Rayleigh wave phase velocities, *J. Geophys. Res.*, *102*(B11), 24,469–24,483, doi:10.1029/97JB02156.
Lawrence, J. F., and D. A. Wiens (2004), Combined receiver-function and surface wave phase-velocity inversion using a niching genetic algorithm: application to Patagonia, *Bull. Seismol. Soc. Am.*, *94*(3), 977–987.
Lebedev, S., J. M. C. Adam, and T. Meier (2013), Mapping the Moho with seismic surface waves: A review, resolution analysis, and recommended inversion strategies, *Tectonophysics*, *609*, 377–394.
Lekić, V., and K. M. Fischer (2014), Contrasting lithospheric signatures across the western United States revealed by S_p receiver functions, *Earth Planet. Sci. Lett.*, *402*, 90–98.
Levander, A., and M. S. Miller (2012), Evolutionary aspects of lithosphere discontinuity structure in the western US, *Geochem. Geophys. Geosyst.*, *13*, Q0AK07, doi:10.1029/2012GC004056.
Levander, A., B. Schmandt, M. S. Miller, K. Liu, K. E. Karlstrom, R. S. Crow, C.-T. Lee, and E. D. Humphreys (2011), Continuing Colorado plateau uplift by delamination-style convective lithospheric downwelling, *Nature*, *472*(7344), 461–465.
Levshin, A. L., and M. H. Ritzwoller (2001), Automated detection, extraction, and measurement of regional surface waves, *Pure Appl. Geophys.*, *158*(8), 1531–1545.
Li, P., and G. Lin (2014), Adaptive ambient noise tomography and its application to the Garlock Fault, Southern California, *Geophys. J. Int.*, p.ggu073.
Liang, C., and C. A. Langston (2008), Ambient seismic noise tomography and structure of eastern North America, *J. Geophys. Res.*, *113*, B03309, doi:10.1029/2007JB005350.
Liang, C., and C. A. Langston (2009), Three-dimensional crustal structure of eastern North America extracted from ambient noise, *J. Geophys. Res.*, *114*, B03310, doi:10.1029/2008JB005919.
Ligorria, J. P., and C. J. Ammon (1999), Iterative deconvolution and receiver-function estimation, *Bull. Seismol. Soc. Am.*, *89*(5), 1395–1400.
Lin, F., M. P. Moschetti, and M. H. Ritzwoller (2008), Surface wave tomography of the western United States from ambient seismic noise: Rayleigh and Love wave phase velocity maps, *Geophys. J. Int.*, doi:10.1111/j1365-246X.2008.03720.x.
Lin, F. C., and M. H. Ritzwoller (2011), Helmholtz surface wave tomography for isotropic and azimuthally anisotropic structure, *Geophys. J. Int.*, *186*, 1104–1120, doi:10.1111/j.1365-246X.2011.05070.x.
Lin, F. C., V. C. Tsai, and B. Schmandt (2014), 3-D crustal structure of the western United States: Application of Rayleigh-wave ellipticity extracted from noise cross-correlations, *Geophys. J. Int.*, *198*, 656–670.
Lin, F.-C., M. H. Ritzwoller, and R. Snieder (2009), Eikonal tomography: Surface wave tomography by phase-front tracking across a regional broad-band seismic array, *Geophys. J. Int.*, *177*(3), 1091–1110.
Lin, F. C., M. H. Ritzwoller, Y. Yang, M. P. Moschetti, and M. J. Fouch (2011), Complex and variable crustal and uppermost mantle seismic anisotropy in the western United States, *Nat. Geosci.*, *4*(1), 55–61.

Lin, F. C., B. Schmandt, and V. C. Tsai (2012a), Joint inversion of Rayleigh wave phase velocity and ellipticity using USArray: Constraining velocity and density structure in the upper crust, *Geophys. Res. Lett.*, *39*, L12303, doi:10.1029/2012GL052196.
Lin, F.-C., V. Tsai, and M. H. Ritzwoller (2012b), The local amplification of surface waves: A new observable to constrain elastic velocities, density, and anelastic attenuation, *J. Geophys. Res.*, *117*, B06302, doi:10.1029/2012JB009208.
Lin, F.-C., and B. Schmandt (2014), Upper crustal azimuthal anisotropy across the contiguous US determined by Rayleigh wave ellipticity, *Geophys. Res. Lett.*, *41*, 8301–8307, doi:10.1002/2014GL062362.
Liu, K., A. Levander, Y. Zhai, R. W. Porritt, and R. M. Allen (2012), Asthenospheric flow and lithospheric evolution near the Mendocino Triple Junction, *Earth Planet. Sci. Lett.*, *323*, 60–71.
Liu, Q.-Y., Y. Li, J. H. Chen, R. D. Van Der Hilst, B. Guo, J. Wang, S. H. Qi, and S. C. Li (2010), Joint inversion of receiver function and ambient noise based on Bayesian theory, *Chin. J. Geophys.*, *53*(6), 961–972.
Ma, S., G. A. Prieto, and G. C. Beroza (2008), Testing community velocity models for Southern California using the ambient seismic field, *Bull. Seismol. Soc. Am.*, *98*(6), 2694–2714.
Maceira, M., and C. J. Ammon (2009), Joint inversion of surface wave velocity and gravity observations and its application to central Asian basins shear velocity structure, *J. Geophys. Res.*, *114*, B02314, doi:10.1029/2007JB005157.
Mooney, W. D., and M. K. Kaban (2010), The North American upper mantle: Density, composition, and evolution, *J. Geophys. Res.*, *115*, B12424, doi:10.1029/2010JB000866.
Mordret, A., N. M. Shapiro, S. Singh, P. Roux, J. P. Montagner, and O. Barkved (2013), Azimuthal anisotropy at Valhall: The Helmholtz equation approach, *Geophys. Res. Lett.*, *40*, 2636–2641, doi:10.1002/grl.50447.
Moschetti, M. P., M. H. Ritzwoller, and N. M. Shapiro (2007), Surface wave tomography of the western United States from ambient seismic noise: Rayleigh wave group velocity maps, *Geochem. Geophys. Geosyst.*, *8*, Q08010, doi:10.1029/2007GC001655.
Moschetti, M. P., M. H. Ritzwoller, and F. C. Lin (2010a), Seismic evidence for widespread crustal deformation caused by extension in the western USA, *Nature*, *464*(7290), 885–889.
Moschetti, M. P., M. H. Ritzwoller, F. C. Lin, and Y. Yang (2010b), Crustal shear velocity structure of the western US inferred from ambient noise and earthquake data, *J. Geophys. Res.*, *115*, B10306, doi:10.1029/2010JB007448.
Mosegaard, K., and A. Tarantola (1995), Monte Carlo sampling of solutions to inverse problems, *J. Geophys. Res.*, *100*(B7), 12,431–12,447, doi:10.1029/94JB03097.
Obrebski, M., R. Allen, F. F. Pollitz, and S.-H. Hung (2011), Lithosphere-asthenosphere interaction beneath the western US from the joint inversion of body-wave travel times and surface-wave phase velocities, *Geophys. J. Int.*, *185*, 1003–1021.
Özalaybey, S., M. K. Savage, A. F. Sheehan, J. N. Louie, and J. N. Brune (1997), Shear-wave velocity structure in the northern Basin and Range Province from the combined analysis of receiver functions and surface waves, *Bull. Seismol. Soc. Am.*, *87*(1), 183–199.
Parker, E. H., R. B. Hawman, K. M. Fischer, and L. S. Wagner (2013), Crustal evolution across the southern Appalachians: Initial results from the SESAME broadband array, *Geophys. Res. Lett.*, *40*, 3853–3857, doi:10.1002/grl.50761.
Pedersen, H. A., P. Boue, P. Poli, and A. Colombi (2015), Arrival angle anomalies of Rayleigh waves observed at a broadband array: A systematic study based on earthquake data, full waveform simulations and noise correlations, *Geophys. J. Int.*, *203*(3), 1626–1641, doi:10.1093/gji/ggv382.
Pollitz, F. F., and W. D. Mooney (2014), Seismic structure of the Central US crust and shallow upper mantle: Uniqueness of the Reelfoot Rift, *Earth Planet. Sci. Lett.*, *402*, 157–166.
Pollitz, F. F., and J. A. Snoke (2010), Rayleigh-wave phase-velocity maps and three-dimensional shear-velocity structure of the western US from local non-plane surface-wave tomography, *Geophys. J. Int.*, *180*, 1153–1169.
Porritt, R. W., R. M. Allen, D. C. Boyarko, and M. R. Brudzinski (2011), Investigation of Cascadia segmentation with ambient noise tomography, *Earth Planet. Sci. Lett.*, *309*(1), 67–76.
Porritt, R. W., R. M. Allen, and F. F. Pollitz (2014), Seismic imaging east of the Rocky Mountains with USArray, *Earth Planet. Sci. Lett.*, doi:10.1016/j.epsl.2013.10.034.
Porter, R., Y. Liu, and W. E. Holt (2015), Lithospheric records of orogeny within the continental US, *Geophys. Res. Lett.*, *43*, 144–153, doi:10.1002/2015GL066950.
Porter, R. C., M. J. Fouch, and N. C. Schmerr (2014), Dynamic lithosphere within the Great Basin, *Geochem. Geophys. Geosyst.*, *15*, 1128–1146, doi:10.1002/2013GC005151.
Prieto, G. A., and G. C. Beroza (2008), Earthquake ground motion prediction using the ambient seismic field, *Geophys. Res. Lett.*, *35*, L14304, doi:10.1029/2008GL034428
Ritzwoller, M. H., F. C. Lin, and W. Shen (2011), Ambient noise tomography with a large seismic array, *C. R. Geosci.*, *343*(8), 558–570.
Sabra, K. G., P. Gerstoft, P. Roux, W. A. Kuperman, and M. C. Fehler (2005), Surface wave tomography from microseisms in Southern California, *Geophys. Res. Lett.*, *32*, L14311, doi:10.1029/2005GL023155
Schmandt, B., and F.-C. Lin (2014), *P* and *S* wave tomography of the mantle beneath the United States, *Geophys. Res. Lett.*, *41*, 6342–6349, doi:10.1002/2014GL061231.
Shapiro, N. M., and M. H. Ritzwoller (2002), Monte-Carlo inversion for a global shear-velocity model of the crust and upper mantle, *Geophys. J. Int.*, *151*(1), 88–105.
Shapiro, N. M., M. Campillo, L. Stehly, and M. H. Ritzwoller (2005), High resolution surface wave tomography from ambient seismic noise, *Science*, *307*(5715), 1615–1618.
Shen, W., M. H. Ritzwoller, and V. Schulte-Pelkum (2013a), A 3-D model of the crust and uppermost mantle beneath the central and western US by joint inversion of receiver functions and surface wave dispersion, *J. Geophys. Res. Solid Earth*, *118*, 262–276, doi:10.1029/2012JB009602.
Shen, W., M. H. Ritzwoller, V. Schulte-Pelkum, and F.-C. Lin (2013b), Joint inversion of surface wave dispersion and receiver functions: A Bayesian Monte-Carlo approach, *Geophys. J. Int.*, *192*, 807–836, doi:10.1093/gji/ggs050.
Shen, W., M. H. Ritzwoller, and V. Schulte-Pelkum (2013c), Crustal and uppermost mantle structure in the central US encompassing the Midcontinent Rift, *J. Geophys. Res. Solid Earth*, *118*, 4325–4344, doi:10.1002/jgrb.50321.
Stachnik, J. C., K. Dueker, D. L. Schutt, and H. Yuan (2008), Imaging Yellowstone plume-lithosphere interactions from inversion of ballistic and diffusive Rayleigh wave dispersion and crustal thickness data, *Geochem. Geophys. Geosyst.*, *9*, Q06004, doi:10.1029/2008GC001992.
Tanimoto, T., and L. Rivera (2008), The ZH ratio method for long-period seismic data: Sensitivity kernels and observational techniques, *Geophys. J. Int.*, *172*(1), 187–198.
Taylor, S. R., P. Gerstoft and M. C. Fehler (2009), Estimating site amplification factors from ambient noise, *Geophys. Res. Lett.*, *36*, L09303, doi:10.1029/2009GL037838.
Thurner, S., R. Margolis, A. Levander, and F. Niu (2015), PdS receiver function evidence for crustal scale thrusting, relic subduction, and mafic underplating in the Trans-Hudson Orogen and Yavapai Province, *Earth Planet. Sci. Lett.*, *426*, 13–22.

Tian, Y., W. Shen, and M. H. Ritzwoller (2013), Crustal and uppermost mantle shear velocity structure adjacent to the Juan de Fuca Ridge from ambient seismic noise, *Geochem. Geophys. Geosyst.*, *14*, 3221–3233, doi:10.1002/ggge.20206.

Tibuleac, I. M., and D. von Seggern (2012), Crust-mantle boundary reflectors in Nevada from ambient seismic noise autocorrelations, *Geophys. J. Int.*, *189*(1), 493–500.

Tokam, A. P. K., C. T. Tabod, A. A. Nyblade, J. Julià, D. A. Wiens, and M. E. Pasyanos (2010), Structure of the crust beneath Cameroon, West Africa, from the joint inversion of Rayleigh wave group velocities and receiver functions, *Geophys. J. Int.*, *183*(2), 1061–1076.

Trabant, C., A. R. Hutko, M. Bahavar, R. Karstens, T. Ahern, and R. Aster (2012), Data products at the IRIS DMC: Stepping-stones for research and other application, *Seismol. Res. Lett.*, *83*(6), 846–854, doi:10.1785/0220120032.

Wagner, L. S., K. Stewart, and K. Metcalf (2012), Crustal-scale shortening structures beneath the Blue Ridge Mountains, North Carolina, USA, *Lithosphere*, *4*(3), 242–256.

Wilson, D. C., R. Aster, S. Grand, J. Ni, and W. S. Baldridge (2010), High-resolution receiver function imaging reveals Colorado Plateau lithospheric architecture and mantle-supported topography, *Geophys. Res. Lett.*, *37*, L20313, doi:10.1029/2010GL044799.

Xie, J., M. H. Ritzwoller, W. Shen, Y. Yang, Y. Zheng, and L. Zhou (2013), Crustal radial anisotropy across eastern Tibet and the western Yangtze Craton, *J. Geophys. Res. Solid Earth*, *118*, 4226–4252, doi:10.1002/jgrb.50296.

Xie, J., M. H. Ritzwoller, S. Brownlee, and B. Hacker (2015), Inferring the oriented elastic tensor from surface wave observations: Preliminary application across the western US, *Geophys. J. Int.*, *201*, 996–1021.

Yang, Y. (2014), Application of teleseismic long-period surface waves from ambient noise in regional surface wave tomography: A case study in western USA, *Geophys. J. Int.*, *198*(3), 1644–1652.

Yang, Y., M. H. Ritzwoller, F.-C. Lin, M. P. Moschetti, and N. M. Shapiro (2008), The structure of the crust and uppermost mantle beneath the western US revealed by ambient noise and earthquake tomography, *J. Geophys. Res.*, *113*, B12310, doi:10.1029/2008JB005833.

Yang, Y., M. H. Ritzwoller, and C. H. Jones (2011), Crustal structure determined from ambient noise tomography near the magmatic centers of the Coso region, southeastern California, *Geochem. Geophys. Geosyst.*, *12*, Q02009, doi:10.1029/2010GC003362.

Yao, H., R. D. van Der Hilst, and V. Maarten (2006), Surface-wave array tomography in SE Tibet from ambient seismic noise and two-station analysis—I. Phase velocity maps, *Geophys. J. Int.*, *166*(2), 732–744.

Yeck, W. L., A. F. Sheehan, M. L. Anderson, E. A. Erslev, K. C. Miller, and C. S. Siddoway (2014), Structure of the Bighorn Mountain region, Wyoming, from teleseismic receiver function analysis: Implications for the kinematics of Laramide shortening, *J. Geophys. Res. Solid Earth*, *119*, 7028–7042, doi:10.1002/2013JB010769.

Zhou, L., J. Xie, W. Shen, Y. Zheng, Y. Yang, H. Shi, and M. H. Ritzwoller (2012), The structure of the crust and uppermost mantle beneath south China from ambient noise and earthquake tomography, *Geophys. J. Int.*, doi:10.1111/j.1365-246X.2012.05423.x.

Zhu, L., and H. Kanamori (2000), Moho depth variation in Southern California from teleseismic receiver functions, *J. Geophys. Res.*, *105*(B2), 2969–2980, doi:10.1029/1999JB900322.

Zigone, D., Y. Ben-Zion, M. Campillo, and P. Roux (2015), Seismic tomography of the Southern California plate boundary region from noise-based Rayleigh and Love waves, *Pure Appl. Geophys.*, *172*(5), 1007–1032.